



Research papers

Data fusion of satellite imagery and downscaling for generating highly fine-scale precipitation



Xiang Zhang ^{a,b,c,d,*}, Yu Song ^{a,b,c}, Won-Ho Nam ^e, Tailai Huang ^{a,b,c}, Xihui Gu ^{f,g,*},
Jiangyuan Zeng ^d, Shuzhe Huang ^h, Nengcheng Chen ^{a,b}, Zhao Yan ^a, Dev Niyogi ⁱ

^a National Engineering Research Center of Geographic Information System, School of Geography and Information Engineering, China University of Geosciences, Wuhan 430074, China

^b Hubei Luojia Laboratory, Wuhan 430079, China

^c SongShan Laboratory, Zhengzhou 450046, China

^d State Key Laboratory of Remote Sensing Science, Aerospace Information Research Institute, Chinese Academy of Sciences, Beijing 100101, China

^e School of Social Safety and Systems Engineering, Institute of Agricultural Environmental Science, National Agricultural Water Research Center, Hankyong National University, Anseong, Republic of Korea

^f Department of Atmospheric Science, School of Environmental Studies, China University of Geosciences, Wuhan 430074, China

^g Centre for Severe Weather and Climate and Hydro-geological Hazards, Wuhan 430074, China

^h State Key Laboratory of Information Engineering in Surveying, Mapping, and Remote Sensing (LIESMARS), Wuhan University, Wuhan 430079, China

ⁱ Department of Geological Sciences, Jackson School of Geosciences, and Department of Civil, Architecture, and Environmental Engineering, University of Texas at Austin, Austin, TX 78712, USA

ARTICLE INFO

ABSTRACT

Keywords:

Precipitation

Fusion

IMERG

TMPA

PERSIANN-CDR

Ground data

Random forest

Due to the frequent occurrence of extreme precipitation events on a global scale, accurate estimation of regional precipitation has emerged as a critical concern. Specifically, region-scale hydrological modeling demands precipitation data with high spatiotemporal resolution and precision. Existing research has primarily concentrated on the correction and spatial downscaling of precipitation products. However, a considerable challenge persists in concurrently generating precipitation data with three key characteristics: high precision, high spatiotemporal resolution, and high spatial coverage (termed '3H'). This entails the provision of daily precipitation data at no more than a 1 km resolution, encompassing a full spatial extent. To address this challenge and obtain 3H precipitation data for regional hydrology research, this study introduces a multi-source precipitation data fusion and downscaling approach known as the 'Generate high Resolution, Accurate, Seamless data using Point-Surface (GRASPS) fusion method. This method combines the strengths of several satellite and model data sources to

Abbreviations: 3H, High precision, High resolution and High spatio-temporal continuous; ANN, Artificial Neural Network; CDF, Cumulative Distribution Function; CERES, Clouds and the Earth's Radiant Energy System; CHIRPS, Climate Hazards group InfraRed Precipitation with Station data; CHRS, Center for Hydrometeorology and Remote Sensing; CMA, China Meteorological Administration; DEM, Digital Elevation Model; DT, Decision Tree; EHEs, Extreme Hydrological Events; ERA-5, European Centre for Medium-Range Weather Forecasts Reanalysis v5; GDA, Geographic Difference Analysis; GEO, Geostationary Earth Orbiting; GPCP, Global Precipitation Climatology Project; GPM, Global Precipitation Measurement; GRASPS, Generate high Resolution, Accurate, Seamless data using Point-Surface fusion; IDW, Inverse Distance Weighted; IMERG, Integrated Multi-satellite Retrievals for Global Precipitation Measurement; IR, InfraRed; ISCCP, International Satellite Cloud Climatology Project; KNN, K-Nearest Neighbor; LEO, Low Earth Orbit; LIS, Lighting Imaging Sensor; MAE, Mean Absolute Error; MSWEP, Multi-Source Weighted-Ensemble Precipitation; MOD13Q1, MODIS/Terra Vegetation Indices 16-Day L3 Global 250m SIN Grid; MODIS, Moderate Resolution Imaging Spectroradiometer; NCEP, National Centers for Environmental Prediction; NDVI, Normalized Difference Vegetation Index; NDVI₁₆, the NDVI with a time lag of 16 days relative to precipitation; PCC, Pearson Correlation Coefficient; PERSIANN, Precipitation Estimation from Remotely Sensed Information using Artificial Neural Networks; PERSIANN-CDR, Precipitation Estimation from Remotely Sensed Information using Artificial Neural Networks – Climate Data Record; PMW, Passive/active Microwave; PR, Precipitation Radar; RA, Regression Analysis; RF, Random Forest; RMSE, Root Mean Squared Error; SVM, Support Vector Machine; TCC, Total Cloud Cover; TCH, Three-Cornered Hat; TMI, TRMM Microwave Imager; TMPA, Tropical Rainfall Measuring Mission Satellite Multi-Satellite Precipitation Analysis; TRMM, Tropical Rainfall Measuring Mission Satellite; USGS, the United States Geological Survey; VCI, Vegetation Condition Index; VIRS, Visible and Infrared Scanner; WUA, Wuhan Urban Agglomeration.

* Corresponding authors at: National Engineering Research Center of Geographic Information System, School of Geography and Information Engineering, China University of Geosciences (Wuhan), Wuhan 430074, China (X. Zhang); Department of Atmospheric Science, School of Environmental Studies, China University of Geosciences, Wuhan 430074, China (X. Gu).

E-mail addresses: zhangxiang76@cug.edu.cn (X. Zhang), guxihui421@163.com (X. Gu).

<https://doi.org/10.1016/j.jhydrol.2024.130665>

Received 3 March 2023; Received in revised form 25 December 2023; Accepted 27 December 2023

Available online 26 January 2024

022-1694/© 2024 Elsevier B.V. All rights reserved.

produce a more precise precipitation dataset at a daily scale and 1 km resolution, covering the Wuhan Urban Agglomeration. These sources include the Integrated Multi-satellitE Retrievals for Global Precipitation Measurement (IMERG) from the Global Precipitation Measurement (GPM) mission, Tropical Rainfall Measuring Mission (TRMM) Multi-satellite Precipitation Analysis (TMPA), and Precipitation Estimation from Remotely Sensed Information using Artificial Neural Networks – Climate Data Record (PERSIANN-CDR). Validation against precipitation data from 36 ground gauges yielded a Pearson Correlation Coefficient of 0.77, with Root Mean Squared Error, Mean Absolute Error, and Bias reduced to 6.08 mm, 2.20 mm, and -0.13 mm, respectively. Compared to prior studies, this research not only improved the spatial resolution of the precipitation dataset to 1 km but also enhanced the accuracy of extreme precipitation, resulting in an accuracy increase from 76.92 % to 91.67 %. Additionally, the generated precipitation dataset exhibited excellent performance at both daily and monthly scales. In terms of different land-cover types, the proposed method displayed improved performance in urban areas. Furthermore, the data obtained was subjected to testing across different input variables, precipitation levels, and downscaling algorithms. In conclusion, this study successfully obtained 3H precipitation data to bridge the gap in high-quality and fine-scale precipitation data. The proposed method and the generated dataset hold substantial implications for regional hydrology research and its practical applications.

1. Introduction

Precipitation plays a vital role in the Earth's water cycle, hydrology, meteorology, and agricultural research (Huang et al., 2021; Kotz et al., 2022; Lesk et al., 2020). Accurate estimation of precipitation has long been an important research topic. However, the accurate estimation of precipitation is not a simple task because of its high spatial and temporal variations (Gu et al., 2022; Niu et al., 2022; Wang et al., 2022). Traditional precipitation estimation methods include rainfall gauge measurements, ground weather radar measurements, and satellite remote sensing. Rainfall gauges obtain high-precision data, but they are limited by terrain heterogeneity and relatively high costs, resulting in uneven and sparse distributions at both global and regional scales (Xiong et al., 2021). Ground weather radar obtains atmospheric rainfall information by analyzing radar echo signals; however, the detection range of this method is limited, and its accuracy is greatly affected by environmental and climatic conditions (Hasan et al., 2016; Wang et al., 2018). A pioneering study on ground weather radar precipitation corrected by gauge precipitation demonstrated promising results (Sinclair and Pegram, 2005), but as mentioned previously, the large variance in radar data accuracy remains a problem. Satellite remote sensing based on visible light, InfraRed (IR), Passive/active Microwave (PMW), and multisensor joint inversion has been widely used to detect precipitation. The commonly used remote sensing-based precipitation data include the Integrated Multi-satellitE Retrievals for Global Precipitation Measurement (IMERG) from the Global Precipitation Measurement (GPM) mission, Tropical Rainfall Measuring Mission (TRMM) Multi-satellite Precipitation Analysis (TMPA), Climate Hazards group InfraRed Precipitation with Station data (CHIRPS), Precipitation Estimation from Remotely Sensed Information using Artificial Neural Networks (PERSIANN) and PERSIANN – Climate Data Record (PERSIANN-CDR), etc. In particular, PERSIANN-CDR is generated from the PERSIANN algorithm using GridSat-B1 infrared data and adjusted using the Global Precipitation Climatology Project (GPCP) monthly product to maintain consistency of the two datasets at 2.5° monthly scale throughout the entire record. The most important characteristic of these remote sensing based datasets is the global-wide spatial coverage (Parajuli et al., 2021), and their accuracy are influenced by atmospheric conditions and the inversion algorithms. The spatial resolution of typical satellite precipitation product is approximately 0.1° or 0.25° (Du et al., 2022; Wang et al., 2022). Although some products have higher resolutions, for example, the Climate Prediction Center morphing is 8 km, its accuracy is still insufficient to meet the needs of fine-scale hydrological and climate research (Heymsfield et al., 2018; Sadeghi et al., 2021; Sekaranom and Masunaga, 2019).

Given the above situation, none of the above-mentioned methods alone fully satisfies the 3H data requirements, that is, high precision, high spatiotemporal resolution, and high spatial coverage (e.g., daily precipitation data at no more than 1 km resolution with full spatial

coverage) (Huang et al., 2022a). Given that, the post-processing method deserves more attention. The current methods mainly focus on fusing diverse precipitation datasets to obtain improved data (Chen et al., 2022; Ma et al., 2021; Wu et al., 2020). This method is based on the following three assumptions: 1) The precipitation data measured by rain gauges are highly accurate and represent the actual precipitation values (Xu et al., 2021); 2) Satellite precipitation products are biased on the whole, but can contain useful information about spatio-temporal patterns of precipitation; and 3) the combination of different precipitation products and rain gauge data is more promising for reflecting the temporal and spatial variations of precipitation than a single source precipitation product.

Based on the above assumptions, the current fusion methods are divided into two categories: traditional mathematical approaches and machine learning methods (Lei et al., 2022; Manz et al., 2016; Nerini et al., 2015; Wang et al., 2023a). Traditional mathematical approaches primarily rely on interpolation and regression to fuse and correct precipitation data. One instance is the Multi-Source Weighted-Ensemble Precipitation (MSWEP) model developed by Beck et al. (2017). This model combines satellite, reanalysis, and station data by introducing the cumulative distribution function (CDF) and P-frequency correction techniques (Beck et al., 2019). The new precipitation data has a spatial resolution ranging from 0.1° to 0.25° and a temporal resolution of 3 h. Similarly, Cheema and Bastiaanssen (2011) used regression analysis (RA) and geographic difference analysis (GDA) to correct TRMM data in the Indus River Basin and found that the annual deviation decreased from 10.90 % to 6.10 %, while the monthly deviation decreased from 34.90 % to 15.40 %. In recent studies, Xu et al. (2020a) used the three-cornered hat (TCH) method to perform a weighted fusion of global precipitation datasets at multiple monthly and daily scales, and the generated dataset had a decreased random error at each temporal scale. In recent years, machine learning has been adopted to directly utilize multiple precipitation datasets (Chivers et al., 2020; Gunning et al., 2019; Zandi et al., 2022). For example, Wu et al. (2020) used CNN-LSTM to downscale Tropical Rainfall Measuring Mission Satellite (TRMM) and thermal infrared data from 2001 to 2005 in China, then obtained precipitation products with a spatial resolution of 0.05°. Compared to the original TRMM products, the root mean square error and mean absolute error decreased by 17.00 % and 14.70 %, respectively.

Although a great progress has been made in satellite precipitation correction, previous studies have mainly concentrated on large-scale areas, such as river basins or countries, and most of their spatial resolutions are up to 0.05° (Shen et al., 2019; Xu et al., 2020a). Meanwhile, global urban regions, e.g., urban agglomerations have rapidly expanded in recent years. Under the influence of global warming and heat/dry island effects, extreme weather events occur frequently (Kunkel et al., 2020; Yuan et al. 2022), thus, high-quality 3H regional precipitation data are urgently required (Xu et al., 2020b). However, the resolutions of current precipitation products are relatively coarse for this size of

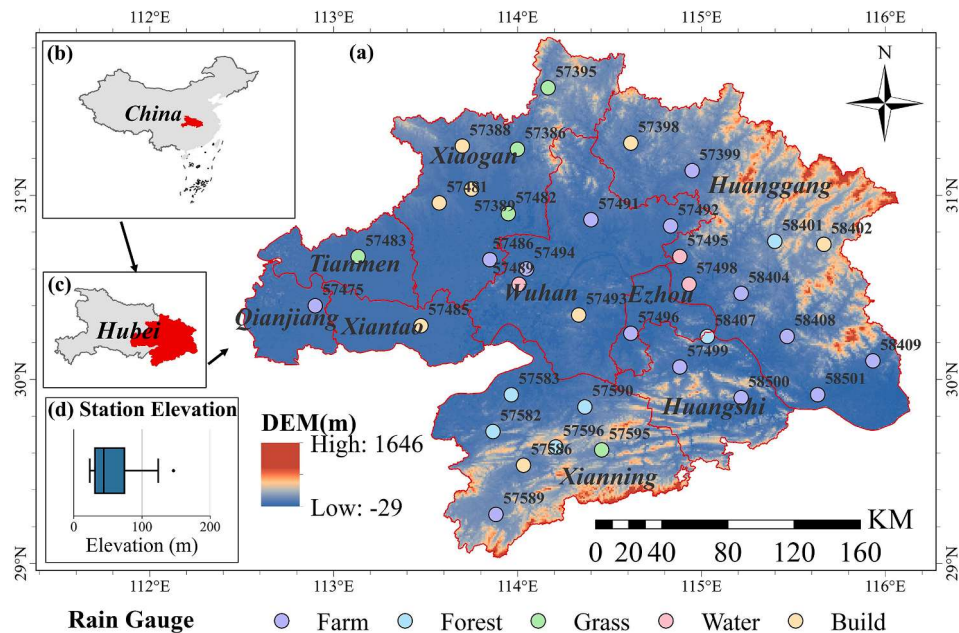


Fig. 1. The geographical location of WUA. The dots in Fig. 1 (a) represent the locations of the national-level rain gauges selected for this study. The color of each point represents the land cover type at that location. The legend from blue to brown in the study area represents the changes in elevation from low (-29 m above sea level.) to high (1646 m above sea level.). Fig. 1 (b) shows the location of Hubei Province in China. Fig. 1 (c) shows the location of WUA in Hubei Province. Fig. 1 (d) shows the elevation distribution of these rain gauges. (For interpretation of the references to color in this figure legend, the reader is referred to the web version of this article.)

Table 1

The datasets used in this study. The table contains the name, version, temporal resolution, spatial resolution, and reference of the datasets used in this study.

Data and version	Spatial resolution	Temporal resolution	Reference
IMERG (Level 3, V6)	0.1° × 0.1°	Daily	https://disc.gsfc.nasa.gov/datasets/GPM_3IMERGDF_06/ summary
TMTPA (V7)	0.25° × 0.25°	Daily	https://disc.gsfc.nasa.gov/datasets/TRMM_3B42RT_Daily_7/ summary
PERSIANN-CDR	0.25° × 0.25°	Daily	https://chrsdata.eng.uci.edu/
ERA-5 TCC (Cloud)	0.25° × 0.25°	Hourly	https://cds.climate.copernicus.eu/cdssapp#!/dataset/reanalysis-era5-single-levels?tab=form
MOD13Q1 (NDVI)	250 m	16 Days	https://ladsweb.modaps.eosdis.nasa.gov/missions-and-measurements/products/MOD13Q1#overview
DEM	30 m	/	https://www.usgs.gov/centers/eros/science/usgs-eros-archive-digital-elevation-global-30-arc-second-elevation-gtopo30
Ground gauge precipitation	/	Daily	https://www.gisrs.cn/infosordata?id=d7ee8f03-0739-42d2-8e1f-e7a6f20bd961

hydrological and climate studies. Meanwhile, the accuracy of existing correction methods varies depending on the ground gauge coverage and temporal scale (Guo et al., 2020, Luo et al., 2019). To solve these key issues, this study proposes the GRASPS method (Generating high-Resolution, Accurate, Seamless data using Point-Surface fusion) to generate 3H precipitation data. The proposed GRASPS method utilizes the complementary advantages of diverse satellite precipitation products and rain gauge measurements to obtain high-precision, high-resolution (daily and 1 km resolution), and spatially continuous precipitation data. This newly generated data aims to fill the gap in regional scale 3H precipitation data, thereby providing a highly credible

dataset for hydrological research (Chen et al., 2020, Huang et al., 2021). In addition, this work can not only aid in comprehending regional extreme weather and climate mechanisms but also provide valuable information for meteorological disaster prevention and mitigation (Dai et al., 2023, Liu et al., 2022).

2. Study area and data

2.1. Study area

In this study, we selected a typical urban agglomerations area with a population of 31.62 million, the Wuhan Urban Agglomeration (WUA), as our study area, as shown in Fig. 1. The WUA is located in the central and eastern parts of Hubei Province and is a large urban union composed of Wuhan and eight surrounding cities (Huangshi, Ezhou, Xiaogan, Huanggang, Xianning, Xiantao, Qianjiang, and Tianmen). The WUA is located between 29 and 32° N and 112–116.5° E and has a subtropical monsoon climate. This region spans approximately 57,800 km², which means the spatial variations of precipitation are hardly fully represented only by ground meteorology stations. At the same time, rapid urbanization and the formation of urban agglomerations have changed the type and structure of their underlying surfaces, resulting in frequent extreme events, such as heatwaves and waterlogging (Huang et al., 2022b, Lin et al., 2011, Yan et al., 2016, Yuan and Zhai, 2022). Flood and drought issues in the WUA are particularly severe (Chen et al., 2021, Liu and Zhou, 2021). Therefore, high-precision and high-resolution precipitation data is of great importance for studying Extreme Hydrological Events (EHEs) in this region. In addition, the density of the ground gauge was 6 stations/10,000 km² in the WUA, which is sufficient to support precipitation fusion research (Chen et al., 2019, Wu et al., 2020, Zeng et al., 2022). This point will be further discussed in Section 5.3. Given the above considerations, this study takes the WUA as an example to generate 3H precipitation data using the proposed GRASPS method.

2.2. Data

Three types of datasets were selected for precipitation fusion in this study, i.e., multiple satellite precipitation products, precipitation-related data (i.e., cloud cover, vegetation cover, and terrain data), and ground-gauge precipitation data, as shown in Table 1. In particular, three widely used satellite precipitation products were selected: i.e., IMERG, TMPA, and PERSIANN-CDR. A Digital Elevation Model (DEM), Normalized Difference Vegetation Index (NDVI), and cloud cover data for the study area were also selected as relevant variables to represent the potential spatial heterogeneity of precipitation. Considering the temporal heterogeneity of precipitation (i.e., seasonal changes), the corresponding *day* of the year and *month* variables were also added to the method. The impacts of different input variables on the final fusion accuracy will be further discussed in the following sections.

1) Satellite precipitation data.

Previous studies have shown that different satellite products have different precipitation estimation accuracies. Overall, the performances of IMERG and TMPA were better than those of PERSIANN and PERSIANN-CDR, and IMERG performed better in winter based on seasonal analysis. Considering the climatological calibration implemented in the precipitation processing algorithm, the TMPA-3B42RT also performed reasonably well (Gan et al., 2023; Huffman et al., 2010; Islam et al., 2020; Zhang et al., 2023). To compensate for the shortcomings of the current precipitation products while retaining their advantages, three satellite precipitation datasets, IMERG, TMPA, and PERSIANN-CDR, were selected for fusion and correction in this study. In addition, it should be considered that ‘Real-Time’ data and ‘Final’ products represent two distinct but common types of precipitation data, with one including gauge data and the other not. Including both data types in the training dataset could potentially enhance the model’s generalization performance. Consequently, we selected both data types, ‘Real-Time’ TMPA data and ‘Final’ IMERG product, respectively. The details of these three datasets are as follows:

TRMM is the world’s first satellite to carry a rain radar (Huffman et al., 2007), in addition to the Visible and Infrared Scanner (VIRS), TRMM Microwave Imager (TMI), Precipitation Radar (PR), Lighting Imaging Sensor (LIS), Clouds and the Earth’s Radiant Energy System (CERES), and other sensors. It was launched in Japan on November 27, 1997. The TRMM Near Real-Time Precipitation Level 3 Version 07 product was used in this study. This product was generated using the Near Real-Time 3-hourly TRMM Multi-Satellite Precipitation Analysis TMPA (3B42RT) (GES DISC. 2016). The TMPA-3B42RT algorithm involves the conversion of calibrated brightness temperature data from geostationary-orbit infrared sensors into geostationary-orbit infrared estimates. These estimates are then integrated with PMW estimates to generate the TMPA-3B42RT (hereinafter referred to as TMPA) product. The product is characterized by approximately 8 h of latency and a spatial resolution of 0.25°/3 h, covering latitudes from 50°N to 50°S. The TMPA data used in this study covered the period from January 1 to December 31, 2019, with 0.25° and daily resolution.

The Global Precipitation Measurement (GPM) satellite was launched in February 2014 to measure rain and snow. The IMERG algorithm combines information from the GPM satellite constellation to estimate precipitation over most of the Earth’s surface. The system was run several times for each observation time, first providing a quick estimate (IMERG Early Run), and successively providing better estimates as more data arrived (IMERG Late Run). The final step uses monthly gauge data to create research-level products (IMERG Final Run). Level-3 version 06 data from the IMERG Final Run were used in this study (Huffman et al., 2020; Huffman et al. 2019). This version fuses the early precipitation estimates collected in 2000–2014 during the operation of the TRMM satellite with more recent precipitation estimates collected during operation of the GPM satellite. In addition, compared with previous

version, the displacement vectors in version 06 are computed using the Modern Era Retrospective Reanalysis 2 and Goddard Earth observing system model forward processing data instead of the previously used infrared data. The IMERG data used in this study covered the period from January 1 to December 31, 2019, with 0.1° and daily resolution.

The PERSIANN was developed by the Centre for Hydrometeorology and Remote Sensing (CHRS) at the University of California, Irvine (Nguyen et al., 2019). The existing PERSIANN algorithm provides global precipitation estimation using combined IR and PMW information from multiple Geostationary Earth Orbiting (GEO) and Low Earth Orbit (LEO) satellites. PERSIANN-CDR uses infrared satellite data from NOAA’s International Satellite Cloud Climatology Project (ISCCP) dating back to 1979, with a spatial resolution of 0.25° and a daily temporal resolution (Ashouri et al., 2015). In this CDR product, the nonlinear regression parameters of the Artificial Neural Network (ANN) model are trained and remain fixed in order to eliminate the need for PMW observations. The training of the ANN is completed using the National Centers for Environmental Prediction (NCEP) stage IV hourly precipitation data. Furthermore, a bias-adjustment stage based on GPCP 2.5° monthly precipitation data is incorporated into the reconstruction process. This study used data from January 1 to December 31, 2019.

2) Gauge precipitation data.

Gauge precipitation data were obtained from the China Meteorological Administration (CMA) measured by national rain gauges. These rain gauge data were provided at two temporal scales, that is, 12 h and daily scales, and this study selected daily scale data in millimeters. A total of 36 gauges were selected in the study area, with an average density of six stations per 10,000 km². Previous studies have shown that this density of gauges is sufficient to support precipitation-related studies (Chen,et al., 2019; Wu,et al., 2020; Zeng,et al., 2022). The distribution of all the sites is shown in Fig. 1.

3) Precipitation related data.

Previous studies have already shown that there is a close relationship between cold cloud coverage and rainfall on a large scale, with a linear correlation coefficient exceeding 0.8 (Arkin, 1979; Arkin and Meisner, 1987; Richards and Arkin, 1981). Higher cloud cover is usually accompanied by higher precipitation (Senf et al., 2015). Simultaneously, the cloud cover changed notably with time and spatial location. Therefore, in this study, Total Cloud Cover (TCC) data were selected as candidate variables. TCC data was obtained from ERA-5 (Hersbach et al., 1979), which is the proportion of grid boxes covered by clouds. The TCC is a single-layer field calculated from clouds that occur through different model layers of the atmosphere. The cloud fraction ranged from 0 to 1, with a spatial resolution of 0.25° and a temporal resolution of per hour from January 1, 2019, to December 31, 2019.

At the same time, the growth of vegetation also has a nonnegligible impact on regional precipitation. NDVI is commonly used to represent the growth status of vegetation in a certain region. Therefore, it is used as a proxy to reflect the potential impact of vegetation on precipitation. The NDVI data used in this study was obtained from the Moderate Resolution Imaging Spectroradiometer (MODIS) vegetation condition index (VCI) MODIS Terra product MOD13Q1. It had a spatial resolution of 250 m and was generated every 16 d from January 1 to December 31, 2019.

The DEM reflects the elevation change in a region and is extremely important to represent topographic features. The precipitation distribution is considerably affected by geographical and topographic features. Therefore, this study selected DEM as an auxiliary variable, which was obtained from the United States Geological Survey (USGS) with a spatial resolution of 30 m.

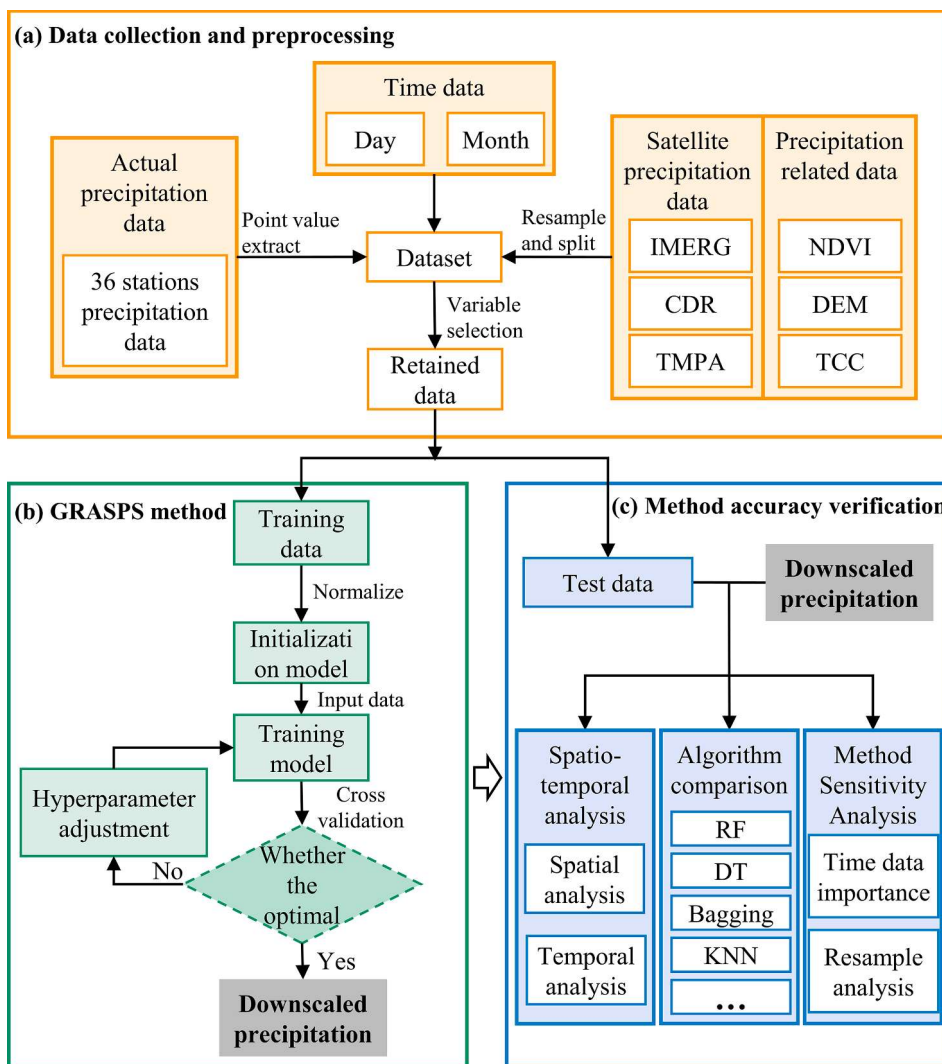


Fig. 2. The methodology of precipitation downscaling fusion. The whole process is divided into three parts: (a) Data collection and preprocessing; (b) GRASPS method; (c) Method accuracy verification.

3. Methods

3.1. Methodology

The proposed framework for generating high-resolution, high-precision, and continuous spatiotemporal precipitation data is shown in Fig. 2. The overall process was divided into three steps: (a) data collection and preprocessing, (b) GRASPS method execution, and (c) accuracy verification and sensitivity testing. First, the selected data were collected and the necessary preprocessing (resampling, cropping, extraction, and dataset segmentation) was performed. Based on this, the downscaling model was trained, data downscaling fusion was performed, and the optimal model was obtained by cross-validation. Subsequently, the trained model and generated downscaling dataset were comprehensively evaluated from various aspects using a variety of evaluation indicators. More detailed information regarding this methodology is provided below.

3.2. Data processing and dataset segmentation

This study used various data sources, including satellite precipitation products, precipitation-related data, and ground-gauge precipitation data. As these data have different spatial and temporal resolutions, processing is necessary. This processing includes eliminating abnormal

data, establishing a unified coordinate system and resolution, resampling, and cutting. To obtain the expected 1 km downscaling precipitation product, all surface data were resampled to 1 km. In particular, bilinear interpolation has been used for resampling, as previous studies have indicated that it performed better in terms of uniform data spatial resolution in precipitation correction (Krishnan et al., 2022, Peng et al., 2019, Shiru et al., 2020, Wang et al., 2023b, Zhang et al., 2018). In Section 5.2, the reliability of this approach is quantitatively evaluated. Subsequently, it was necessary to unify the temporal resolution of all types of data to obtain the expected daily dataset. The original temporal resolution of the cloud cover data was one hour, the mean of 24 cloud cover values from 0:00 UTC to 24:00 UTC per day was calculated as the daily cloud cover data. The original NDVI data had a temporal resolution of 16 days. Previous studies have shown that different vegetation types exhibited lagged response time of 10–16 days or more in relation to precipitation (Zeng et al., 2022). To integrate the NDVI data with precipitation information, it was assumed that the NDVI remained constant within a 16-day period. This assumption allowed us to assign the NDVI value, that is $NDVI_{16}$ to represent the precipitation that occurred during the previous 1st–16th day. This approach effectively maps the precipitation data to the corresponding NDVI values by considering the lag response time of vegetation to rainfall. We are aware that this assumption does not completely match the actual conditions. However, due to the challenges in obtaining high-quality NDVI data on a daily scale, this

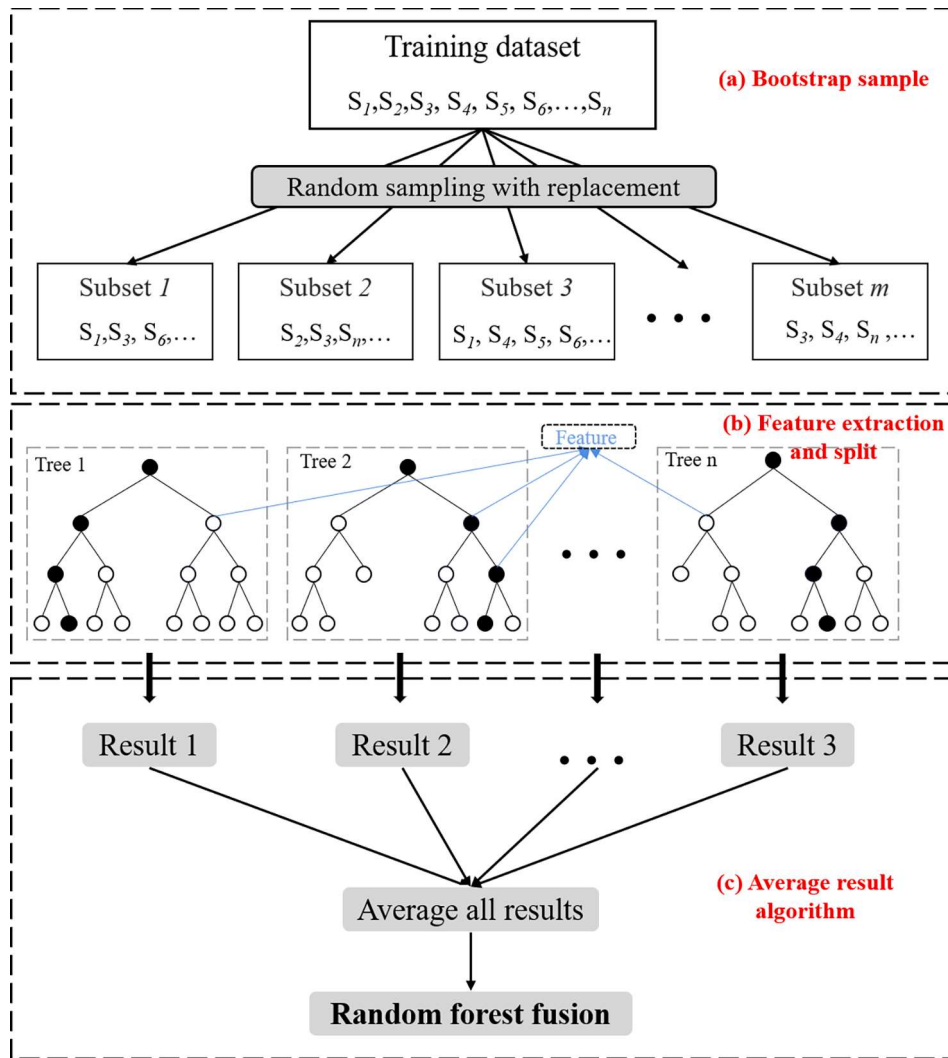


Fig. 3. The structure of the RF model. (a), (b), and (c) represent three specific processes in the model process, the (a) Bootstrap sample, (b) Feature extraction and split, and (c) Average result algorithm, respectively.

Table 2

The equations and detailed information of PCC, RMSE, MAE, and BIAS. x_i and y_i represent the i^{th} downscaled value and ground measurement, respectively. N is the number of the sample.

Metric	Equation	Unit
PCC	$PCC = \frac{N\sum x_i y_i - \sum x_i \sum y_i}{\sqrt{N\sum x_i^2 - (\sum x_i)^2} \sqrt{N\sum y_i^2 - (\sum y_i)^2}}$	—
RMSE	$RMSE = \sqrt{\frac{\sum_{i=1}^N (x_i - y_i)^2}{N}}$	mm
MAE	$MAE = \frac{1}{N} \sum_{i=1}^N (x_i - y_i) $	mm
BIAS	$BIAS = \frac{1}{N} \sum_{i=1}^N (x_i - y_i)$	mm

assumption was introduced to compensate for the NDVI values on missing dates. Besides that, no notable topographic changes occurred during the study period in the WUA according to the Hubei Geological Bureau. In other words, the DEM data for 2019 remained stable. Similar to the processing method of NDVI, the 2019 year-based DEM data were expanded to daily scale data in 2019.

The daily values of each type of data (i.e., IMERG, TMPA, PERSIANN, TCC, NDVI₁₆, and DEM) at the rain gauges are obtained, and the generated dataset was used as the initial dataset. Temporality is integral

to precipitation effects. Although the precipitation dataset contains the effect of temporality, the series of processing steps in the dataset production process may distort this effect. To avoid this potential distortion, this study added the collection month (1–12) of each data point and the corresponding day (1–365) in the whole year of 2019 as separate variables to the input dataset. The importance of these two temporality-related variables is further tested in [Section 5.1](#).

To streamline the model training process and enhance data accuracy, a correlation analysis was conducted between each dataset and the precipitation data collected from rain gauges. Subsequently, the input variables with low correlations were eliminated, as explained in [Section 4.1](#). Finally, the screened dataset was randomly divided into training and verification sets in a 2:1 ratio for model training and verification. In other words, there were 13,140 data in the training set and 4,138 in the test set, respectively.

In this study, we define “one day” as the period from 0:00 Universal Time Coordinated (UTC) on the first day to 0:00 UTC on the second day. IMERG, TMPA, and PERSIANN-CDR are daily-scale data starting at 0:00 UTC. TCC provides hourly data starting at 0:00 UTC on each day. To align with the ‘one day’ definition, we divided TCC into groups of 24 at daily intervals from 0:00 UTC, and we used the group mean as the daily cloud amount. As mentioned earlier in this section, NDVI has a 16-day resolution, but it exhibits relatively minor daily variations, allowing us to treat it as daily NDVI data. We apply a similar approach to DEM

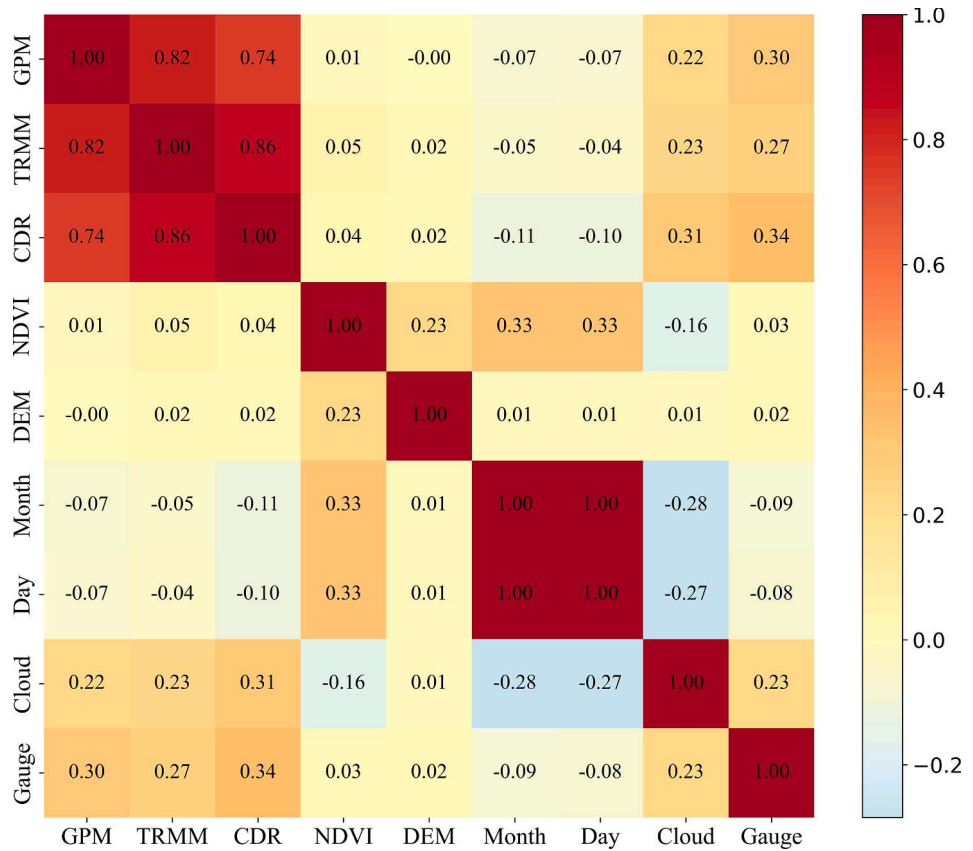


Fig. 4. Pearson correlation coefficient analysis matrix between input variables and gauge measured precipitation. Blue indicates a negative correlation between the input variable and site measured precipitation, red indicates a positive correlation. The darker the color, the higher the correlation. (For interpretation of the references to color in this figure legend, the reader is referred to the web version of this article.)

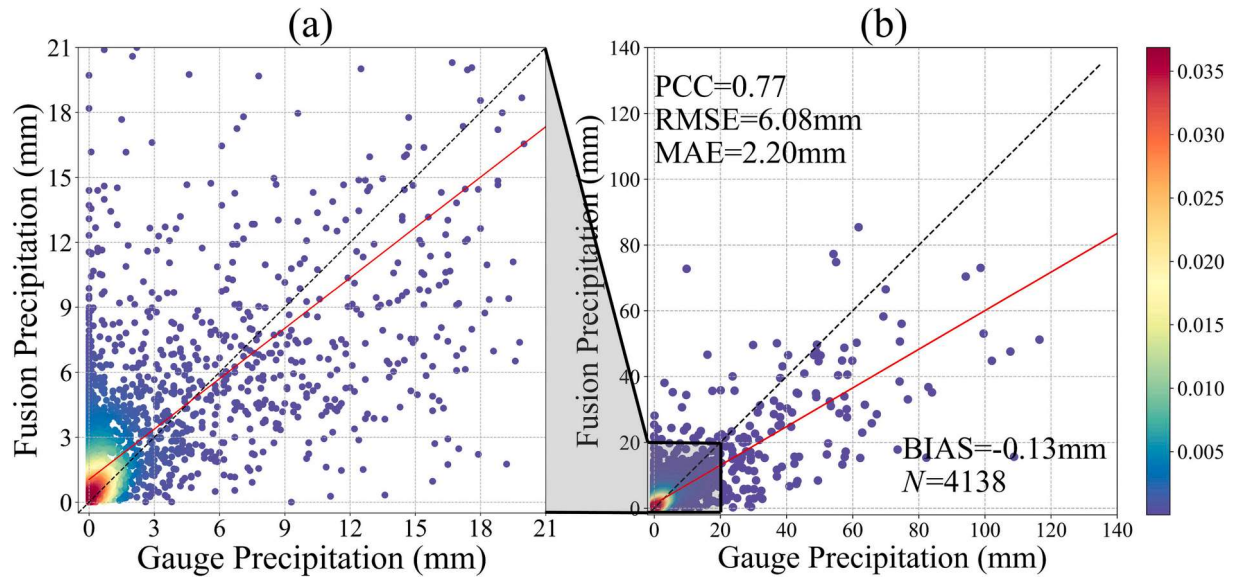


Fig. 5. Scatter plots and evaluation indicators of daily fusion precipitation data and daily ground gauge precipitation data in 2019. The X-axis and Y-axis represent precipitation at ground gauges and fusion precipitation, respectively. The color bar shows the density of the scatter, blue is the sparsest and red is the densest. The dotted line is a 1:1 line, and the red line is a fitted line of the scattered points. PCC, RMSE, MAE, and BIAS represent four evaluation indicators respectively, and N represents the number of scattered points. The Fig. 5 (a) shows a zoomed-in view of the Fig. 5 (b) within the range of 0–20 mm. (For interpretation of the references to color in this figure legend, the reader is referred to the web version of this article.)

and NDVI. Ground precipitation was acquired at 8:00 BJT and 20:00 BJT (i.e., 0:00 UTC and 12:00 UTC) by rain gauges. Data from 0:00 UTC to 0:00 UTC the next day were used for this study. Differences in the spatial

distribution of sites may result in slight errors in the timing of data acquisition. We acknowledge this difference and its potential influence on the results. It's important to note that this data represents the best

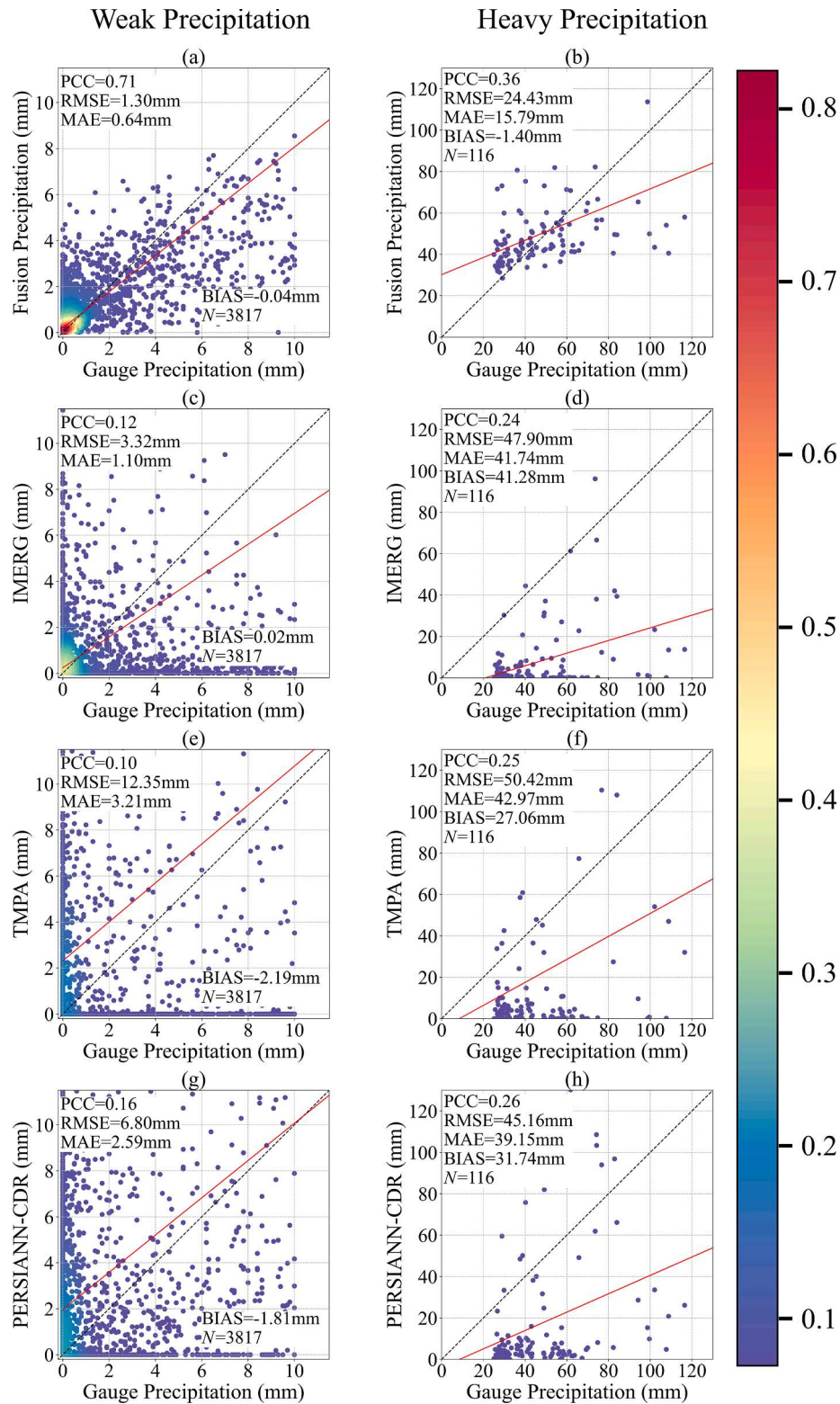


Fig. 6. Scatter plots and evaluation indicators of four daily precipitation datasets (Fusion precipitation, IMERG, TMPA, and PERSIANN-CDR) and daily ground gauge precipitation data under weak and heavy precipitation in 2019. (a), (c), (e), and (g) correspond to the performance of the four datasets during weak precipitation, while (b), (d), (f), and (h) correspond to their performance during heavy precipitation. The X-axis and Y-axis represent precipitation at ground gauges and fusion precipitation, respectively. The color bar shows the density of the scatter, blue is the sparsest, and red is the densest. The dotted line is a 1:1 line, and the red line is a fitted line of the scattered points. PCC, RMSE, MAE, and BIAS represent four evaluation indicators respectively, and N represents the number of scattered points. (For interpretation of the references to color in this figure legend, the reader is referred to the web version of this article.)

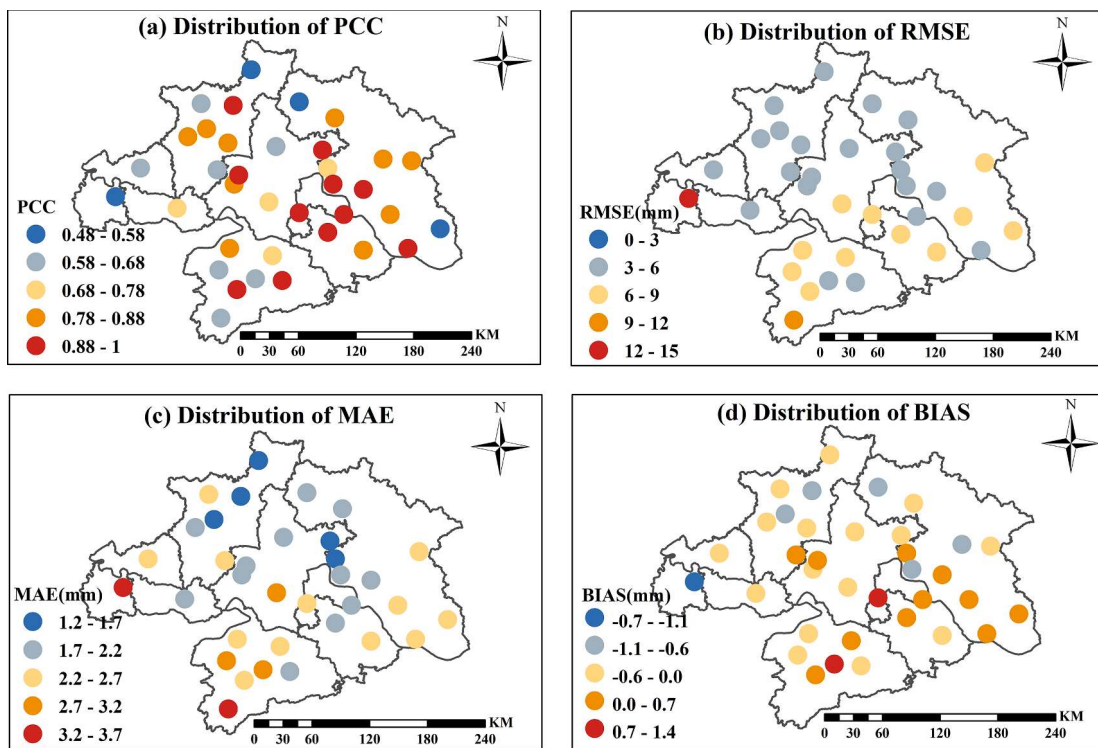


Fig. 7. The spatial distribution of each evaluation metric of fusion precipitation in WUA. (a) PCC, (b) RMSE, (c) MAE, and (d) BIAS.

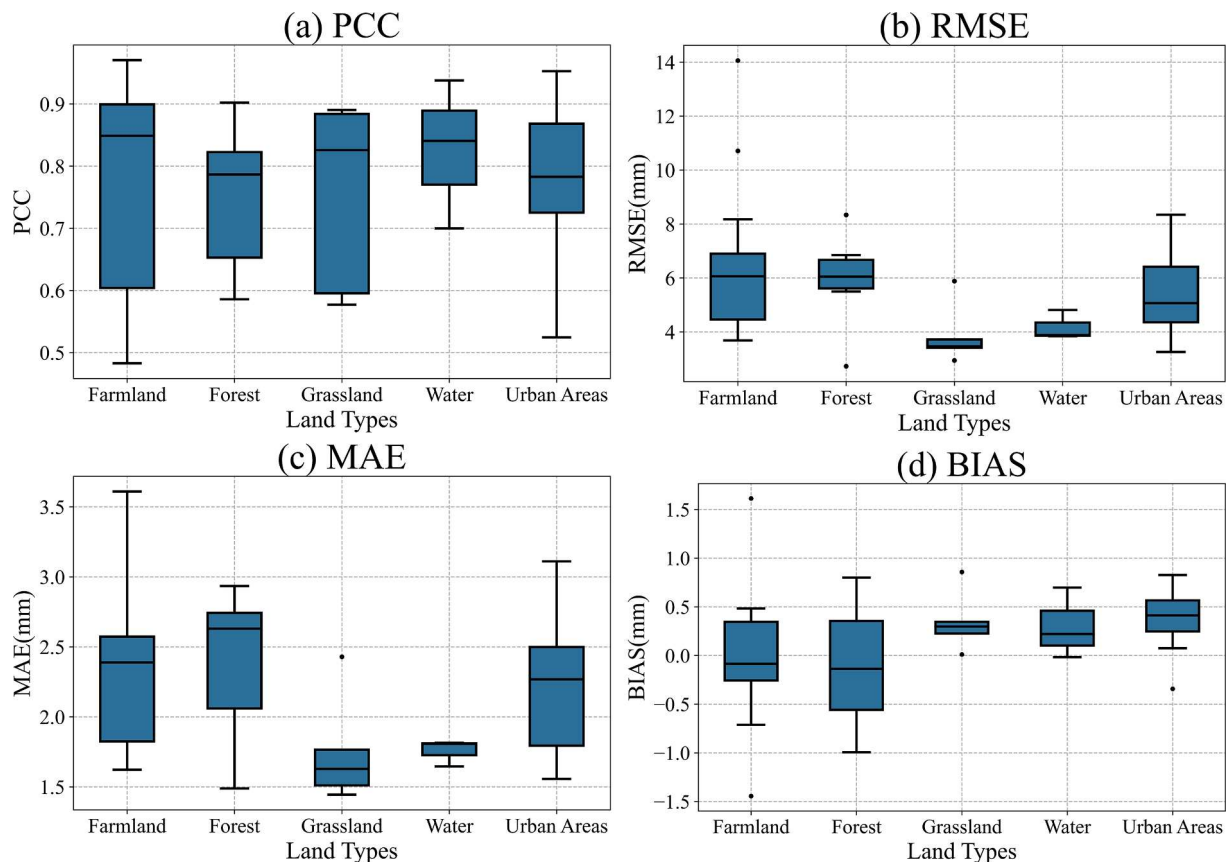


Fig. 8. Evaluation metrics of fusion precipitation in terms of land cover types in WUA. (a) PCC, (b) RMSE, (c) MAE, and (d) BIAS. In each box, the central mark indicates the median, the size of the green box represents the degree of dispersion, and the green points represent outliers. The sample sizes for the five land cover types, namely farm, forest, grassland, water, and built areas, are as follows: 1755, 753, 527, 376, and 727. (For interpretation of the references to color in this figure legend, the reader is referred to the web version of this article.)

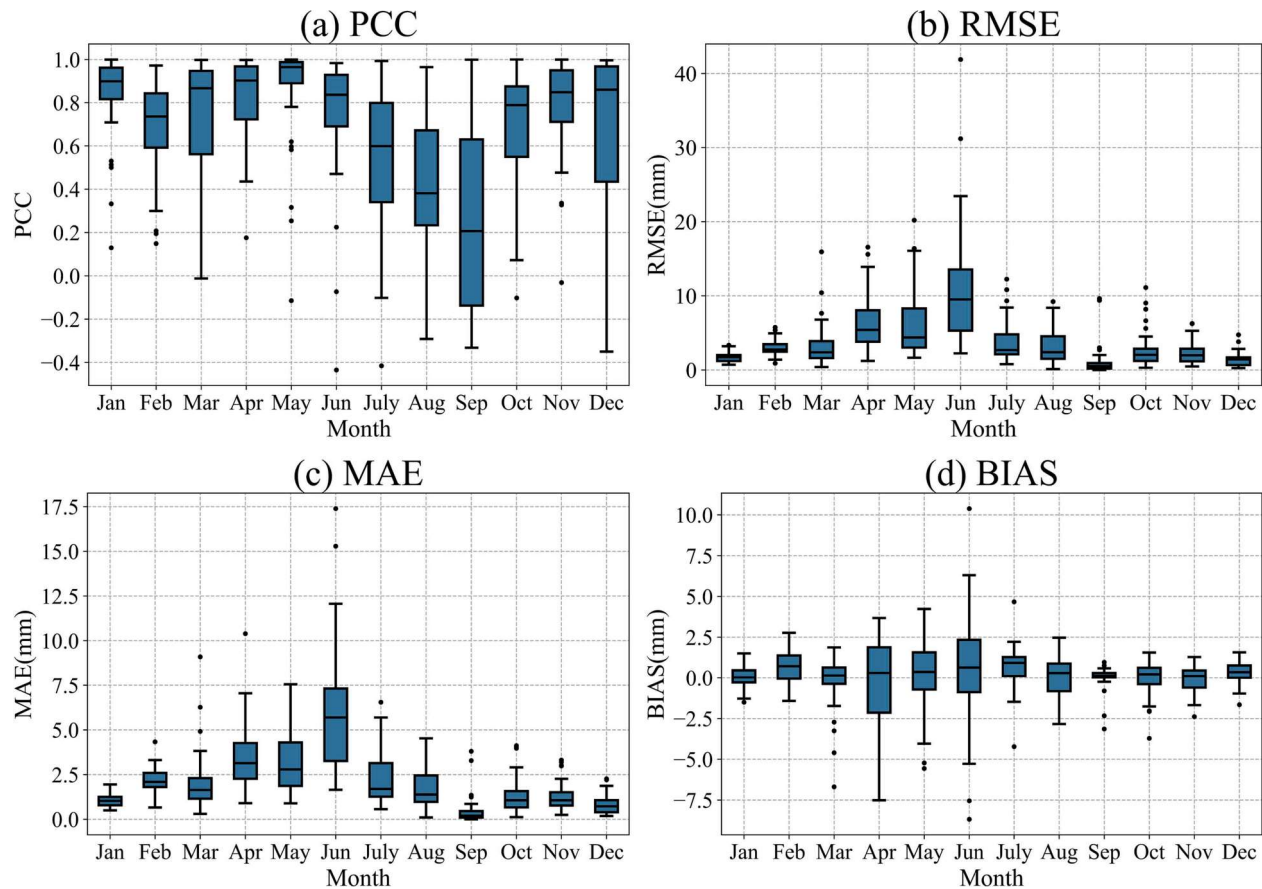


Fig. 9. Evaluation metrics of fusion precipitation over time in WUA. (a) PCC, (b) RMSE, (c) MAE, and (d) BIAS. In each box, the central mark indicates the median, the size of the green box represents the degree of dispersion, and the green points represent outliers. (For interpretation of the references to color in this figure legend, the reader is referred to the web version of this article.)

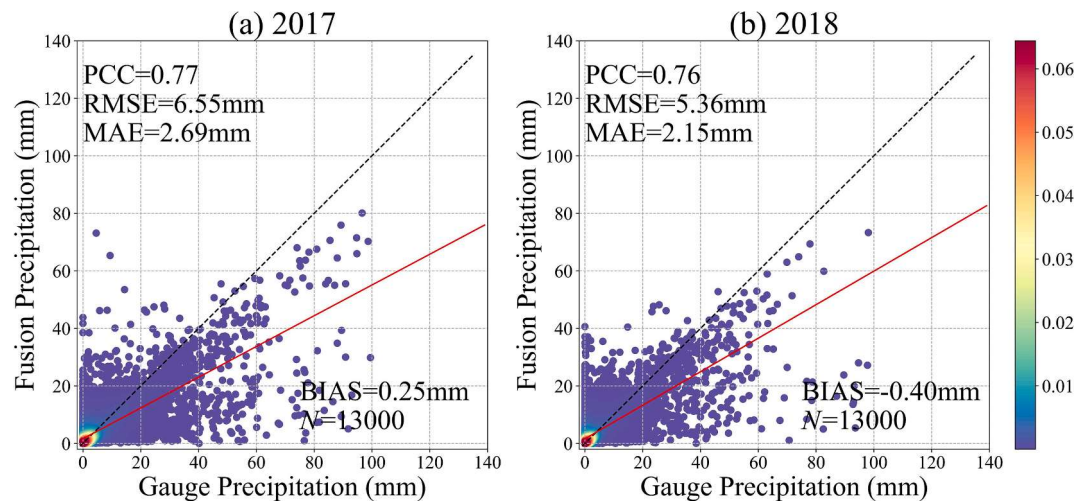


Fig. 10. The applicability of the model at other times (2017 and 2018). (a) 2017. (b) 2018. The X-axis and Y-axis represent precipitation at ground gauges and fusion precipitation, respectively. The color bar shows the density of the scatter, blue is the sparsest, and red is the densest. The dotted line is a 1:1 line, and the red line is a fitted line of the scattered points. PCC, RMSE, MAE, and BIAS represent four evaluation indicators respectively, and N represents the number of scattered points. (For interpretation of the references to color in this figure legend, the reader is referred to the web version of this article.)

available information at present, with previous research confirming its reliability. Our comprehensive results further demonstrate the effectiveness of the proposed method in generating highly detailed precipitation data. Therefore, we believe that these minor discrepancies have limited impact, especially in daily-scale studies (Guo and Tian, 2022;

Zhan et al., 2023).

3.3. Random forest-based GRASPS

The GRASPS method employs pixel-by-pixel fusion of various

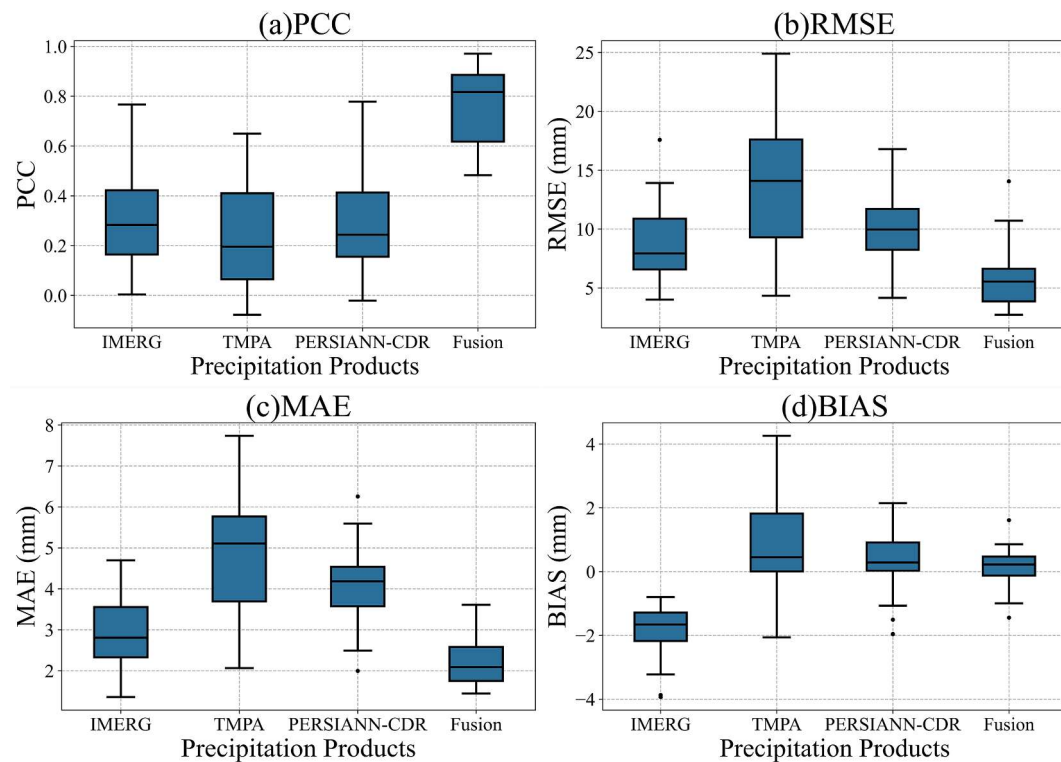


Fig. 11. The evaluation indicators of different precipitation products at all gauges in WUA. (a) PCC, (b) RMSE, (c) MAE, and (d) BIAS. In each box, the central mark indicates the median, the size of the green box represents the degree of dispersion, and the green points represent outliers. (For interpretation of the references to color in this figure legend, the reader is referred to the web version of this article.)

precipitation data products using a random forest algorithm. Random Forest (RF) was introduced by Breiman in 1995 as an ensemble learning algorithm, as depicted in Fig. 3. RF comprises multiple decision trees, with each tree independently learning from and being trained on the sample data. Subsequently, the training results from these trees are combined. Consequently, the combined results surpass those achieved by individual trees. A smaller correlation between these trees leads to a lower error rate in the results, while a stronger regression capability in each tree yields more accurate results. Prior research has also established the effectiveness of RF in enhancing the accuracy of precipitation data (Baez-Villanueva et al., 2020, Wager, 2016, Wolfensberger et al., 2021). The specific training process is as follows:

1) Sample set segmentation

In the bootstrap sampling method, the sample set was repeatedly sampled to obtain N samples for training subsets. Under this approach, samples are randomly selected from the dataset on each iteration, allowing for the possibility that some data may be used in multiple trees while others may never be used. This enables each decision tree to learn from multiple features and to select features from various perspectives, ultimately contributing to the final training result.

2) Build a decision tree.

m features were randomly selected from the training subset as the basis for splitting each node in the decision tree, and a complete decision tree was then grown from the root node from top to bottom. Meanwhile, there is no pruning process for each tree; that is, each tree grows to its maximum.

3) Generate RF.

Repeat Steps 1 and 2 n times to extract n training subsets and

generate N decision trees, Tree 1, Tree 2, ..., Tree n to form an RF.

4) Generate results.

The training samples (IMERG, TMPA, PERSIANN, TCC, NDVI₁₆, and DEM) were input into the RF, and each decision tree obtains a fusion result. Finally, the mean value of all decision-tree fusion results was calculated using the average result algorithm to obtain the final fusion result.

3.4. Method evaluation

To quantitatively evaluate the proposed method and downscaled data, the following four indicators are used, including Pearson Correlation Coefficient (PCC), Root Mean Squared Error (RMSE), Mean Absolute Error (MAE), and BIAS. The details of these four indicators are provided in Table 2.

4. Results and discussion

4.1. Correlation analysis for dependent and independent variables

The PCC was utilized to assess the correlation between each input variable and site-measured precipitation, as depicted in Fig. 4. In terms of correlation, IMERG, TMPA, and PERSIANN-CDR displayed higher PCC values (0.30, 0.27, and 0.34, respectively) compared to other variables. Statistically significant results were determined using a p-value threshold of < 0.05 , and no statistically significant differences at this level were observed among the various sample sets. Additionally, PCC values between the original satellite precipitation and ground gauge precipitation were generally below 0.35 but notably higher than the other auxiliary variables. The PCC values between these three satellite precipitation datasets ranged from 0.74 to 0.86, suggesting the inversion results of different satellite precipitation data exhibited both similarities

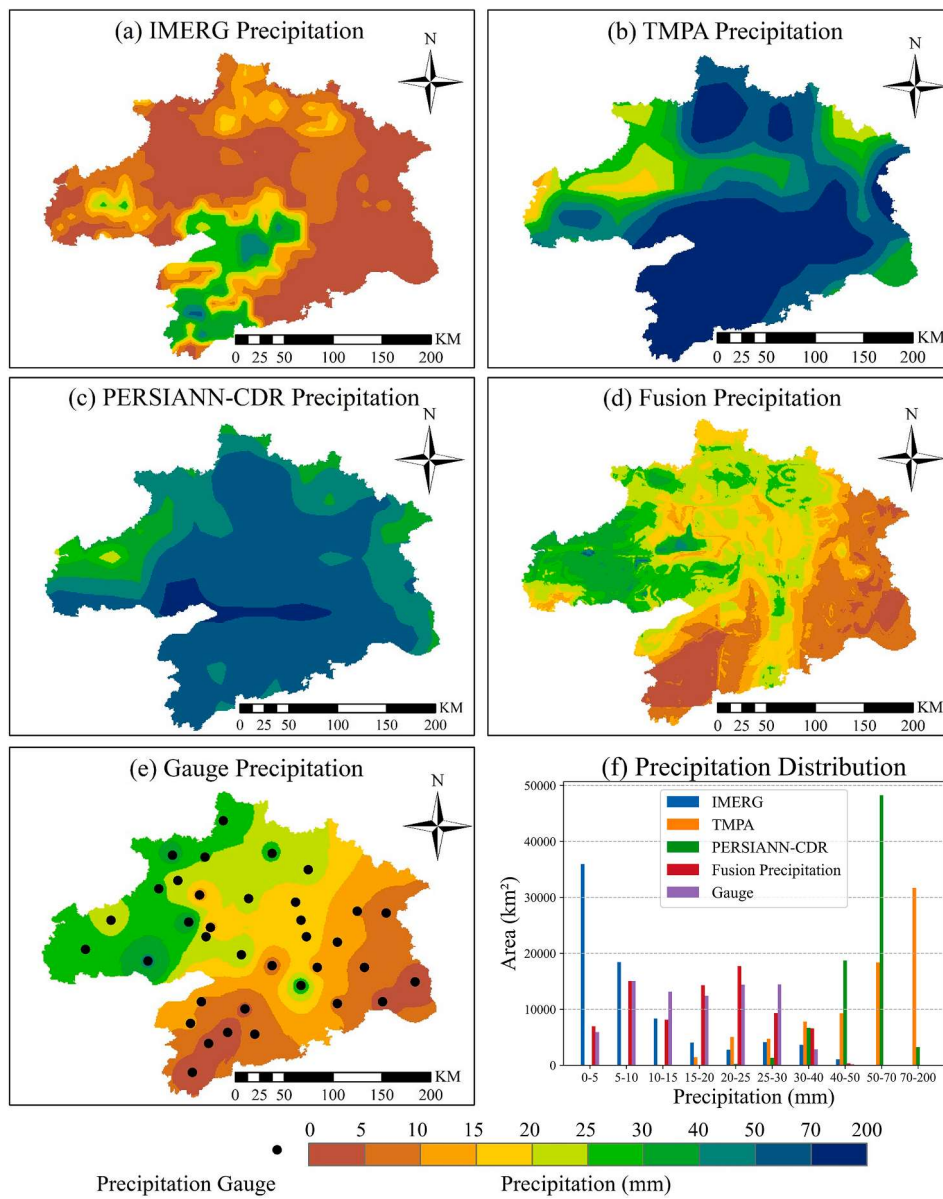


Fig. 12. Comparison of the spatial distribution of precipitation before and after downscaling. (a)–(c) are the precipitation results of IMERG, TMPA, and PERSIANN-CDR before downscaling, respectively. (d) is the downscaling fusion result. (e) is the interpolation result of precipitation at the site. (f) is the area occupied by different precipitation in (a)–(e).

and differences. Two temporally-related auxiliary variables, namely *month* and *day*, showed weak negative correlations with ground gauge precipitation (-0.09 and -0.08). Among the auxiliary variables, cloud cover data demonstrated the highest PCC (0.23), while DEM and NDVI₁₆ exhibited the lowest PCC values (0.02 and 0.03, respectively). It is worth noting that NDVI₁₆ is a product of NDVI expansion processing, which doesn't fully correspond to the actual lag time, resulting in its lower correlation with real precipitation. Furthermore, the elevation differences among various meteorological stations, except station 57596, were relatively inconspicuous, with a standard deviation of elevation at 33.72 m, leading to a low PCC for DEM (Fig. 1-Station Ele). To streamline model training and eliminate the influence of low-correlation data, the two variables with the weakest correlations, NDVI₁₆ and DEM, were excluded from subsequent experiments. The remaining six variables, namely IMERG, TMPA, PERSIANN-CDR, Cloud, Month, and Day, were employed for model training.

To optimize model performance, the hyperparameters were iteratively adjusted during the training phase. Previous studies have

highlighted the impact of two hyperparameters, *n_estimators* and *max_depth*, on the RF model (Mokhtar et al., 2021). Considering the volume of training data in this study, we conducted extensive testing of the following two hyperparameters during the model tuning stage, i.e., *n_estimators* (100, 200, 300, 500, 700, 1000, and 2000) and *max_depth* (5, 10, 15, 20, 25, 30, and 50). Our experiment revealed that the model achieved the optimal performance when *n_estimators* was set to 200 and *max_depth* was set to 20.

4.2. Performance of the downscaled precipitation by GRAPS

4.2.1. Verification of the accuracy of fused precipitation

The trained model was employed to fuse previously validated inputs to quantitatively assess the accuracy of the proposed method. The results, depicted in Fig. 5, illustrate the performance as evaluated through four key indicators: Pearson Correlation Coefficient (PCC), Root Mean Squared Error (RMSE), Mean Absolute Error (MAE), and BIAS. The scatter densities in the plots are derived from the Gaussian kernel

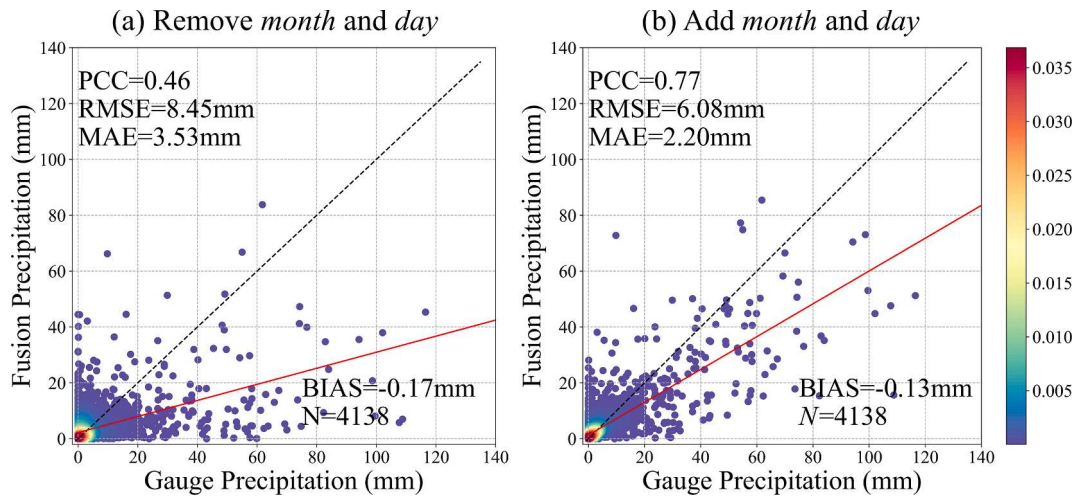


Fig. 13. Temporal Data Importance Analysis. (a) Remove month and day. (b) Add month and day. The X-axis and Y-axis represent precipitation at ground gauges and fusion precipitation, respectively. The color bar shows the density of the scatter, blue is the sparsest, and red is the densest. The dotted line is a 1:1 line, and the red line is a fitted line of the scattered points. PCC, RMSE, MAE, and BIAS represent four evaluation indicators respectively, and N represents the number of scattered points. (For interpretation of the references to color in this figure legend, the reader is referred to the web version of this article.)

density function, representing the number of points per square unit. This pattern is consistent across all scatter plots in the text. A total of 4138 data points were subjected to model testing, with precipitation values ranging from 0 to 120 mm/day and an average daily precipitation of 2.82 mm. The overall PCC for the proposed model was 0.77, marking an impressive improvement of 126.47 % to 185.19 % compared to the original satellite precipitation data products in Fig. 4. The values for RMSE, MAE, and BIAS were notably low, with measurements of 6.08 mm, 2.20 mm, and -0.13 mm, respectively. In summary, these results demonstrate that the GRASPS fusion method exhibits outstanding performance with high precision at a spatial resolution of 1 km.

To further investigate the downscaling fusion performance at each ground gauge location, a scatter density map analysis was conducted as depicted in Fig. A1. The method was evaluated using 115 data points for each site, and the analysis revealed distinct scatter density distributions at different ground sites, suggesting spatial variability in the model's performance. For instance, sites 57492, 57586, and 58404 exhibited the highest Pearson Correlation Coefficient (PCC) values, all exceeding 0.95. However, sites 57398 and 58409 showed lower PCC values of 0.52 and 0.50, respectively. Additionally, despite sites 57386 and 58401 having correlation coefficients above 0.80, they displayed negative BIAS values of -0.86 mm and -0.80 mm, indicating an underestimation of precipitation. Among the 36 gauges, 22 had negative BIAS values, while 14 had positive BIAS values, aligning with the overall analysis that suggests a slight underestimation of precipitation by the model.

As depicted in Fig. 5, the performance of the downscaling fusion method exhibited variations under different precipitation conditions. To further evaluate its performance under extremely low and high precipitation conditions, we segmented the test dataset based on the rainfall rating criteria established by the CMA. Specifically, we categorized precipitation levels of 0–10 mm/day as 'weak precipitation' and those exceeding 25 mm/day as 'heavy precipitation.' We subsequently analyzed the fusion results for both precipitation categories, as illustrated in Fig. 6. Across all test datasets, we identified 3817 cases of weak precipitation (0–10 mm/day) and 116 cases of heavy precipitation (>25 mm/day). The average daily precipitation for weak precipitation cases was 0.74 mm/day, in contrast to the 48.90 mm/day recorded for heavy precipitation cases. Notably, the quantity of weak precipitation data cases was approximately 30 times greater than that of heavy precipitation data cases. The Pearson Correlation Coefficient (PCC) for the fusion precipitation in extreme precipitation scenarios was 0.71 and 0.36, respectively, which was slightly lower than the overall precipitation

scenarios depicted in Fig. 5. This decline in PCC underscores the inherent difficulty in accurately estimating extreme precipitation. Furthermore, the two error indicators, RMSE and MAE, in Fig. 6(b) exceeded those in Fig. 6(a), largely due to the amplified errors arising from the intensity of precipitation.

According to the aforementioned CMA rainfall rating criteria, precipitation within the range of [0, 10] mm/day was classified as weak precipitation. Consequently, in Fig. 6(a, c, e and g), weak precipitation includes scenarios where no precipitation occurs (i.e., precipitation measures 0 mm). Among all the test data, instances of no precipitation accounted for 68.10 % of the overall dataset. It's worth noting that rainfall often coincides with cloudy days; however, the presence of cloudy weather does not necessarily entail precipitation. This situation introduces non-negligible uncertainty, particularly when there is minimal or no precipitation aside from cloud cover. Furthermore, since precipitation values are non-negative, their estimation errors possess a robust lower bound but lack a comparable upper bound. Consequently, even if an estimator is impeccably calibrated, it may still exhibit large bias at the lower end, primarily due to noise. As a result, the fused precipitation near 0 mm was overestimated. However, it's notable that the BIAS in weak precipitation was only -0.04 mm, reflecting good performance. Given the inherent challenges associated with monitoring heavy precipitation, the model's performance did decrease in these scenarios. Nonetheless, it managed to improve the PCC by 76.92 % to 91.67 % compared to the original satellite precipitation data, as seen in Fig. 6(c, e and g), which present the comparison results of the three satellite precipitation products and gauge precipitation under heavy precipitation conditions, respectively. The scatter points of the three satellite precipitation products were concentrated near the coordinate axis, suggesting that uncorrected satellite precipitation data struggles to faithfully represent real precipitation conditions. In contrast, the scattered points of the fused precipitation were notably concentrated along the 1:1 line in Fig. 6(a) during heavy precipitation, and this trend was consistently observed in Fig. 6(b, d, f and h) under heavy rainfall conditions. Therefore, the fused precipitation outperformed uncorrected satellite precipitation data in both extreme precipitation scenarios. Overall, the downscaling fusion method demonstrated exceptional performance in scenarios involving extreme precipitation.

4.2.2. Spatial analysis of the graps method

Based on the preceding analysis, it is evident that gauges located at different spatial positions exert varying influences on the downscaling

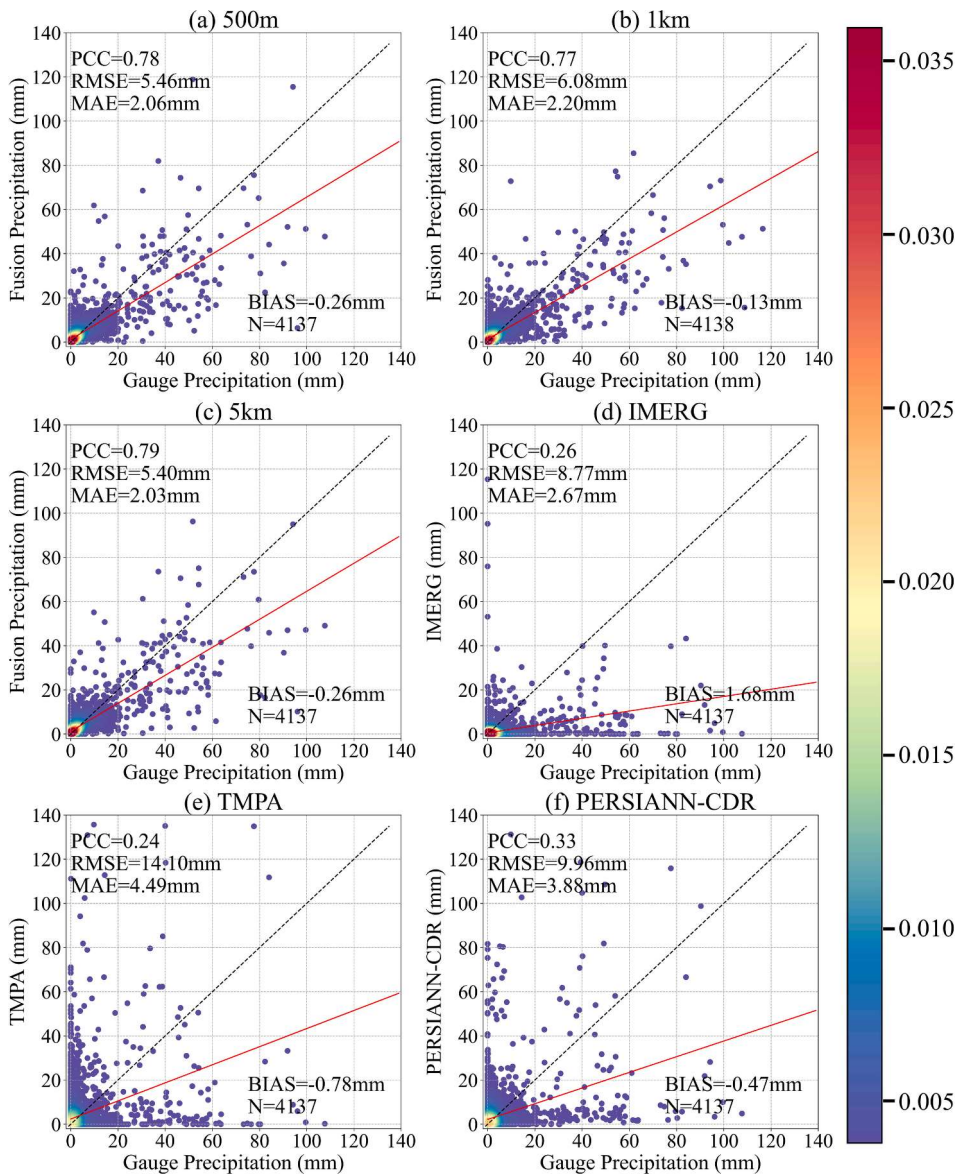


Fig. 14. Resample level analysis. (a) 500 m. (b) 1 km. (c) 5 km. (d) IMERG. (e) TMPA. (f) PERSIANN-CDR. The X-axis and Y-axis represent precipitation at ground gauges and fusion precipitation, respectively. The color bar shows the density of the scatter, blue is the sparsest, and red is the densest. The dotted line is a 1:1 line, and the red line is a fitted line of the scattered points. PCC, RMSE, MAE, and BIAS represent four evaluation indicators respectively, and N represents the number of scattered points. (For interpretation of the references to color in this figure legend, the reader is referred to the web version of this article.)

fusion performance. To delve deeper into these spatial effects, we conducted an analysis of the spatial distributions of those four evaluation metrics, with the results illustrated in Fig. 7. Across all test samples, daily precipitation values ranged from 0 to 120 mm, with an average of 2.82 mm per day. Fig. 7 demonstrated the distribution of the 36 verification sites in the WUA along with the corresponding evaluation metrics of fusion precipitation at these locations. As depicted in Fig. 7(a), the correlation in the southeast region was notably higher than that in the northwest, consistently remaining at or above 0.68, with a majority of values exceeding 0.78. In Fig. 7(b, c and d), the distribution patterns for these three error indicators exhibited uniform trends, all decreasing from southeast to northwest. The overall BIAS in the southeastern region ranged between 0 and 0.70, whereas in the central to northwestern regions of the study area, it varied from -1.10 to 0. In other words, a small portion of the southeastern region exhibited a tendency to overestimate precipitation, while a bigger portion of the central to northwestern region leaned towards underestimating precipitation. This discrepancy may be linked to the topography of the study area. Previous research has

indicated that areas below 3,500 m in elevation are more prone to precipitation underestimation (Jia et al., 2011), and the overall elevation of the WUA stands below 1,646 m.

4.2.3. Influence of different land cover on grasps accuracy

The WUA region comprises five distinct land cover types: farmland, forest, grassland, water bodies, and built-up areas. These land-cover categories accounted for 42.42 %, 18.19 %, 15.15 %, 9.09 %, and 15.15 % of the total area, respectively. To investigate the influence of these diverse land-cover types, we employed four evaluation metrics to assess the performance, as illustrated in Fig. 8. To ensure the accuracy of land cover classification, we visually interpreted the land types at each site using Google Earth. The sites were categorized into five groups: farmland, forest, grassland, water, and urban areas. In Fig. 8(a), the higher degree of box aggregation in built areas suggests that the GRAPS model yields more stable precipitation fusion results for urban regions. Farmland exhibited the highest median PCC; however, it displayed relative discreteness. This can be attributed to the presence of numerous

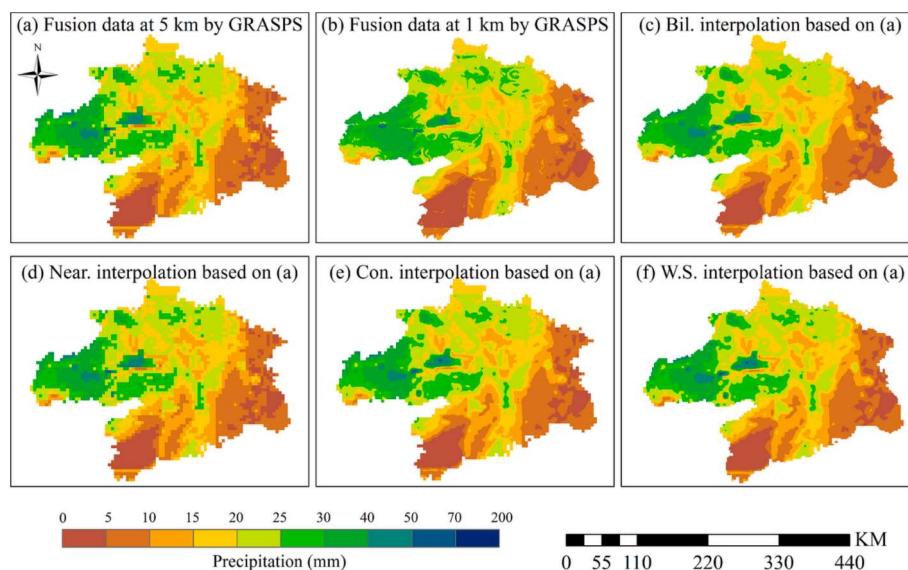


Fig. 15. Comparison of directly interpolated 1 km precipitation data with the fusion data by the proposed GRASPS. (a) is the fusion result at 5 km. (b) is the fusion result of 1 km by GRASPS. (c)-(f) are the results of resampling (a) to 1 km using different resampling algorithms, including the bilinear interpolation, nearest neighbor, cubic convolution, and Lanczos windowed sinc algorithms respectively.

isolated gauges within farmland areas, which are susceptible to human activities and land-use changes. Regarding three accuracy indicators, RMSE in Fig. 8(b), MAE in Fig. 8(c), and BIAS in Fig. 8(d), grassland and water land cover types showed low error values. Nonetheless, given the limited number of meteorological stations available within these land categories, further research is warranted to validate and provide additional evidence for these findings. Meanwhile, gauges situated in farmland and urban areas exhibited minor errors, underscoring the applicability of this downscaling fusion method in towns and urban settings.

4.2.4. Temporal analysis of the graps method

To assess the accuracy of the fusion results over time, we calculated four evaluation metrics and conducted statistical analyses of monthly variations in 2019, as presented in Fig. 9. The PCC of the model exceeded 0.70 in January through June and October through December, surpassing that of July through September. Moreover, the level of aggregation in these months notably exceeded that observed in July through September, signifying more stable model correlations. Within the test dataset, the proportions of no precipitation (i.e., 0 mm) from July to September accounted for 75.35 %, 80.23 %, and 94.36 % of the total data for each respective month. Fig. A2 also clearly illustrates the higher frequency of no-precipitation events from July to September compared to the other months. These findings align with those outlined in Section 4.2.1, underscoring the model's heightened susceptibility to cloud cover and limitations in accuracy when estimating precipitation in the absence of actual precipitation. Consequently, model accuracy diminished during this period, with the PCC declining by approximately 22.07 % to 48.05 %. In Fig. 9(b – d), the RMSE, MAE, and BIAS from April to June registered higher values compared to other months. Notably, BIAS was greater than zero, indicating a slight overestimation of precipitation during this period.

4.2.5. Generalization analysis of the graps method

To assess the model's applicability to other years, we selected data from the study area for the years 2017 and 2018 for comparative experiments. We applied the same GRASPS method in 2017 and 2018 as we did in 2019, resulting in the inclusion of 13,000 data points in the experiment, as depicted in Fig. 10. In 2017, the overall precipitation ranged from 0 to 98.70 mm/day, with an average daily precipitation of 3.63 mm/day. Similarly, in 2018, the overall precipitation ranged from

0 to 94.80 mm/day, with an average daily precipitation of 3.21 mm/day. The fusion data in 2017 yielded the same PCC of 0.77 as observed in 2019. In 2018, although marginally lower, the result was only approximately 0.09 % less. Regarding RMSE and MAE, they measured 6.55 mm and 2.69 mm in 2017, and 5.36 mm and 2.15 mm in 2018, respectively. In comparison to the values of 6.08 mm and 2.20 mm obtained in 2019, the overall high performance remained consistently stable. In validation experiments conducted over different time periods with a larger dataset, the downscaled model produced nearly identical results to the original, underscoring the exceptional generalization capability of GRASPS model and its suitability for longer temporal scales.

4.3. Comparison between current satellite precipitation and GRASPS generated precipitation

4.3.1. Temporal variation comparison between graps data and satellite precipitation data

To assess the generated results against the original satellite precipitation data, we conducted an analysis of fusion precipitation, ground precipitation measurements, and satellite precipitation products (IMERG, TMPA, and PERSIAN-CDR). We randomly selected results from four stations, as illustrated in Figs. A2 – A5. For these four sites, it was observed that TMPA and PERSIAN-CDR data were more inclined to over- or underestimate precipitation values. In contrast, the IMERG and gauge precipitation data exhibited greater consistency, albeit with a slight underestimation. This discrepancy can be attributed to the well-known scale effect that exists between ground measurements and satellite data. Notably, the generated precipitation data demonstrated a high level of agreement with gauge precipitation data, noticeably outperforming the precipitation data derived from the three satellite sources. This outcome underscores the substantial value of the proposed GRASPS method. To delve deeper into the analysis, we selected the period of concentrated precipitation from May 20 to June 30 for further examination. At station-57389, TMPA data accounted for only 30.00 % to 50.00 % of the actual precipitation value, resulting in a noticeable underestimation of precipitation. PERSIAN-CDR data hardly corresponded to actual precipitation, whereas IMERG data exhibited relatively better agreement with actual precipitation but remained less accurate than the fusion precipitation. This pattern was consistent across all stations, indicating that the GRASPS method consistently generated high-quality precipitation data. These findings further substantiate the

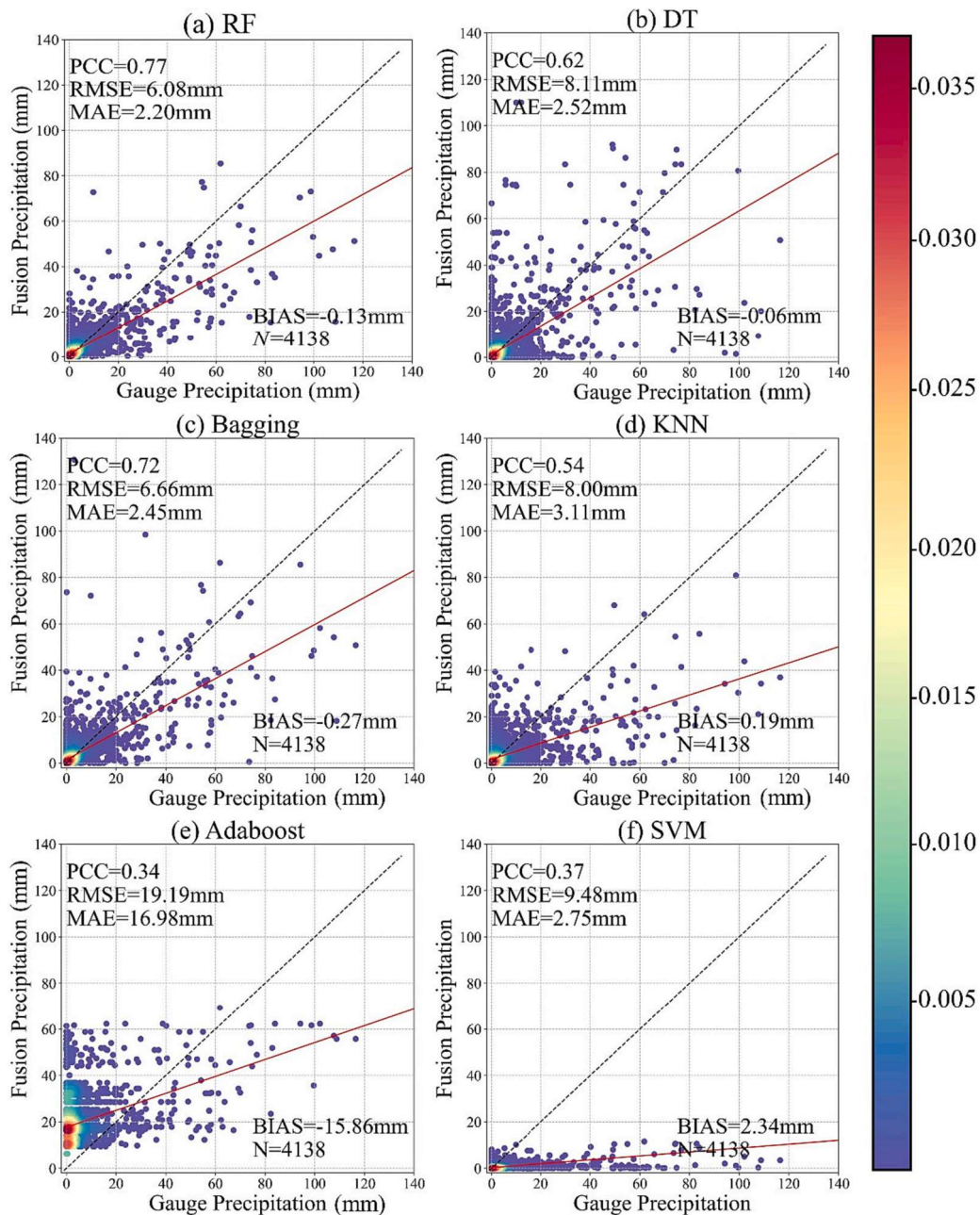


Fig. 16. Comparison of different downscaling algorithms. The X-axis and Y-axis represent precipitation at ground gauges and fusion precipitation, respectively. The color bar shows the density of the scatter, blue is the sparsest, and red is the densest. The dotted line is a 1:1 line, and the red line is a fitted line of the scattered points. PCC, RMSE, MAE, and BIAS represent four evaluation indicators respectively, and N represents the number of scattered points. (For interpretation of the references to color in this figure legend, the reader is referred to the web version of this article.)

effectiveness of the GRASPS method in producing accurate and reliable precipitation data.

4.3.2. Comparison of graps data and satellite precipitation data by performance indicators

To further quantitatively assess the performance of the downscaled fusion data in comparison to the original satellite precipitation data, we calculated and compared evaluation metrics across all 36 gauges, as displayed in Fig. 11. As depicted in Fig. 11(a), the PCCs for the fusion precipitation data at all gauges surpassed those of the three satellite precipitation datasets. In Fig. 11(b and c), the RMSE and MAE error metrics of the fused precipitation data were consistently lower than those of the satellite precipitation datasets, underscoring its superior accuracy. Fig. 11(d) illustrates the BIAS for these four precipitation

datasets, with values fluctuating around the $Y = 0$ line, indicating varying degrees of overestimation or underestimation. Notably, IMERG exhibited a BIAS lower than 0 mm, signifying a substantial underestimation of precipitation by IMERG. It is essential to highlight that the BIAS of the fused precipitation data was the closest to 0 mm among all datasets, underscoring its reliability in comparison to existing satellite precipitation data.

4.3.3. Spatial comparison of graps data and satellite precipitation data

To facilitate a direct comparison between the fusion results and the original satellite precipitation data, we randomly selected downscaling results for June 28, 2019, for a side-by-side evaluation, as presented in Fig. 12. Fig. 12(a – e) displays the spatial distribution of precipitation data, while Fig. 12(f) delineates the distribution of various precipitation

Table 3
The model and hyperparameters.

Model	Hyperparameters	Value
DT	<i>max_depth</i>	None
	<i>min_samples_split</i>	2
	<i>min_samples_leaf</i>	1
	<i>max_features</i>	None
Bagging	<i>n_estimators</i>	10
	<i>max_samples</i>	1.0
	<i>max_features</i>	1.0
KNN	<i>weights</i>	uniform
	<i>p</i>	2
	<i>n_neighbors</i>	5
Adaboost	<i>n_estimators</i>	50
	<i>base_estimator</i>	deprecated
SVM	<i>C</i>	1.0
	<i>gamma</i>	scale
	<i>kernel</i>	rbf
	<i>degree</i>	3

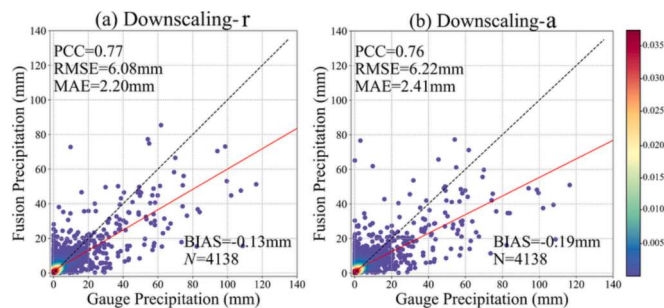


Fig. 17. Comparison of downscaling results of different input variables. DEM and NDVI₁₆ are removed in (a), leaving only IMERG, TMPA, PERSIANN-CDR, Cloud, Month, and Day, here represented as “Downscaling-r”. (b) adds DEM and NDVI₁₆ on the basis of (a), here represented as “Downscaling-a”. The X-axis and Y-axis represent precipitation at ground gauges and fusion precipitation, respectively. The color bar shows the density of the scatter, blue is the sparsest, and red is the densest. The dotted line is a 1:1 line, and the red line is a fitted line of the scattered points. PCC, RMSE, MAE, and BIAS represent four evaluation indicators respectively, and *N* represents the number of scattered points.

amounts across different datasets. Among these, Fig. 12(a–c) represent the original satellite precipitation data. Fig. 12(d) reflects the outcome of fusing the three satellite precipitation datasets using the model developed in this study, with no involvement of gauge precipitation in the generation process. On the other hand, Fig. 12(e) results from the interpolation of gauge precipitation, excluding satellite data from the generation process. Given the comparatively lower spatial resolution of original satellite precipitation data, it was resampled to 1 km using the Inverse Distance Weighted (IDW) method (Duan et al., 2022, Yan et al., 2021) to enable meaningful comparisons. In many instances, satellite precipitation data exhibit a tendency to underestimate heavy precipitation, although exceptions exist. As observed in Fig. 12, IMERG predominantly underestimated actual precipitation, while TMPA and PERSIANN-CDR tended to overestimate it. The fused precipitation data effectively rectified these discrepancies. Notably, the fused data harmoniously blended the spatial distribution trends of IMERG and TMPA, with an emphasis on the two northern regions, offering the closest alignment with ground truth measurements. Fig. 12(f) further illustrated that within the 0–30 mm precipitation range, the downscaled precipitation data closely mirrored the gauge precipitation data,

whereas other datasets exhibited noticeable overestimations of precipitation. This comparison unequivocally underscores the superior reliability of the proposed GRASPS methodology in generating downscaled fusion precipitation data when contrasted with the original satellite data.

4.4. Method sensitivity analysis

4.4.1. Importance analysis on temporal variables in grasps

As expounded in Section 3.2, the impact of temporality on precipitation emerged as a vital consideration. While satellite precipitation data inherently incorporates temporal information, the integrity of this information can be compromised during data processing. Hence, to enhance temporal information, we explicitly introduced *day* and *month* as auxiliary variables into the input datasets. To assess the significance of this inclusion, an experiment was conducted wherein these two temporal data points were removed from the model input, while all other conditions remained constant, as portrayed in Fig. 13. In comparison with Fig. 13(b), the PCC decreased by 40.26 % (PCC = 0.46), and the RMSE (RMSE = 8.45 mm) and MAE (MAE = 3.53 mm) increased by 38.98 % and 60.45 %, respectively, as depicted in Fig. 13(a). These findings unequivocally affirm that the exclusion of temporal data from the model detrimentally affected GRASPS’ capacity to adequately capture temporal variations in precipitation. Consequently, the performance of GRASPS deteriorated in this context, highlighting the necessity of directly incorporating temporal variables into the GRASPS framework.

4.4.2. Resample level analysis in grasps

In this study, the satellite precipitation data were downscaled through resampling to standardize all datasets to a resolution of 1 km. However, a clear consensus regarding the optimal resampling degree remains elusive. It was postulated that a considerable difference in resolution before and after resampling might pose challenges. To address this critical investigation, we conducted a comparative analysis of the fusion results at three distinct resampling levels (500 m, 1 km, and 5 km) in relation to the original satellite precipitation data, as illustrated in Fig. 14. Across these three different scenarios, the PCCs associated with the three resampling scales exhibited variations of no more than 0.01. This consistency underscores the robustness of GRASPS, with nearly uniform results across these different scales. Furthermore, the performance of all three scales notably outperformed that of the original satellite precipitation data. Consequently, this investigation demonstrates that the chosen resampling scale has negligible influence on model performance. Hence, resampling the data to 1 km is a viable approach. Meanwhile, we further directly resampled the fusion results at 5 km to 1 km by multiple interpolation methods and compared them with the fusion results at 1 km, as shown in Fig. 15. It was found the proposed fusion method had efficiently eliminated the uncertainty induced by different interpolation algorithms. This is the advantage when using the proposed GRASPS fusion method.

5. Discussion

5.1. Comparison of different downscaling algorithms

As previously mentioned, two widely utilized downscaling fusion approaches are mathematical methods and machine learning methods (Sachindra et al., 2018, Vandal et al., 2019, Zhang et al., 2021). In this study, we employed Random Forest (RF) as a machine-learning method for downscaling fusion. To assess RF’s role in the downscaling framework, it was subjected to a comparative analysis against several other prominent machine learning algorithms, including Decision Tree (DT), Bootstrap Aggregating (Bagging), K-Nearest Neighbor (KNN), Adaboost, and Support Vector Machine (SVM), using the same validation dataset. The comparative results are presented in Fig. 16. These algorithms were

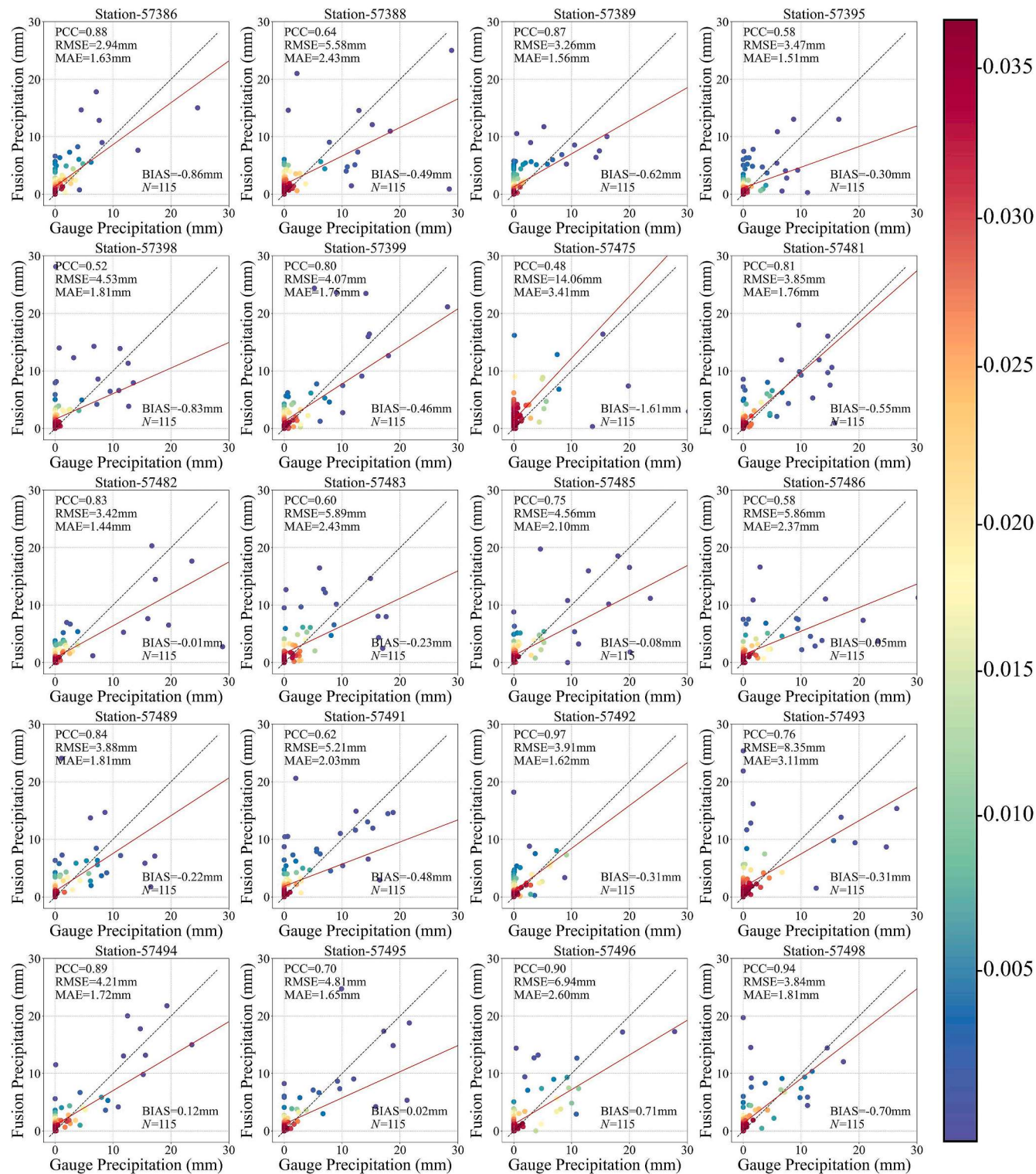


Fig. A1. Scatter plots and evaluation indicators (site-by-site) of daily fusion precipitation data and daily ground gauge precipitation data in 2019. In these figures, X-axis and Y-axis represent precipitation at ground gauges and fusion precipitation, respectively. Scattered points in different colors indicate the intensity of precipitation with red to purple indicating the intensity from dense to sparse, and dotted line is 1:1 line. PCC, RMSE, MAE and BIAS represent four evaluation indicators respectively, and N represents the number of scattered points. The color bar shows the density of the scatter, blue is the sparsest, red is the densest. The dotted line is 1:1 line, and the red line is fitted line of the scattered points.

implemented using the scikit-learn library in Python. Hyperparameters for all algorithms were fine-tuned to attain their optimal values, as outlined in Table 3. In general, the performance metrics of RF, DT, Bagging, and KNN noticeably outperformed those of Adaboost and SVM.

Among the former four algorithms, RF demonstrated superior performance compared to DT and Bagging with respect to the two error indicators, i.e., RMSE and MAE, despite a slightly larger BIAS (-0.13 mm). Specifically, RF reduced RMSE by approximately 5.00 % to 27.00 % and

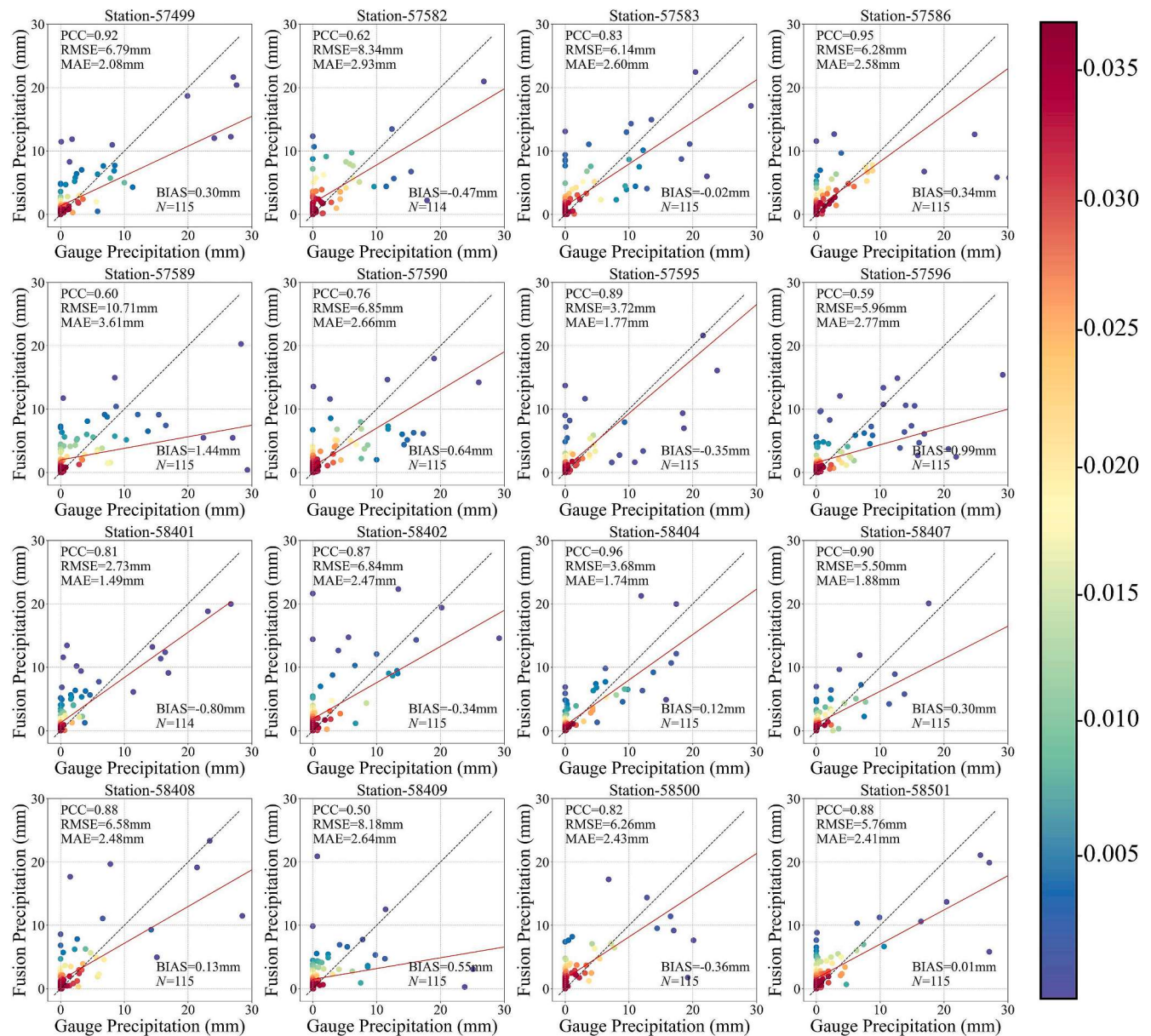


Fig. A1. (continued).

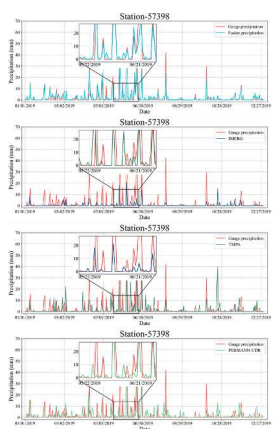


Fig. A2. Temporal evolution of different precipitation datasets for Station-57398 in 2019.

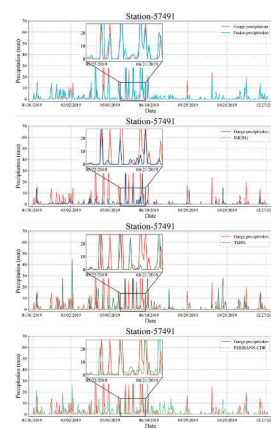


Fig. A3. Temporal evolution of different precipitation datasets for Station-57491 in 2019.

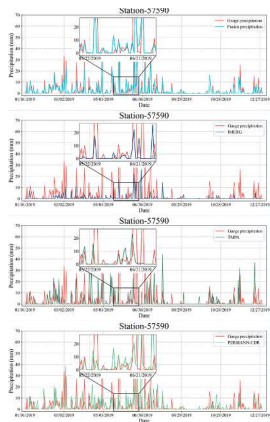


Fig. A4. Temporal evolution of different precipitation datasets for Station-57590 in 2019.

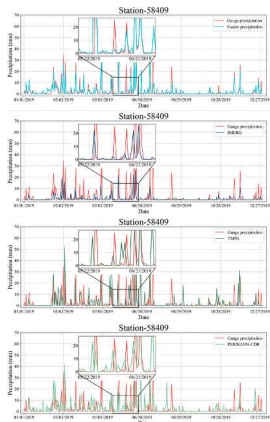


Fig. A5. Temporal evolution of different precipitation datasets for Station-58409 in 2019.

MAE by approximately 3.00 % to 11.00 % in comparison to the other three algorithms. With a PCC of 0.77, RF achieved a PCC approximately 4.00 % to 26.00 % higher than the latter three algorithms. This advantage primarily results from the synergy of DT and Bagging algorithms within RF. RF is a specific implementation of the bagging method, and DT serves as the fundamental component model of RF. Consequently, RF exhibits superior performance relative to individual algorithms. In summary, RF-based GRASPS outperforms other algorithms for precipitation downscaling and fusion.

5.2. Comparison of different input variables

In the preceding experiments, the impact of data redundancy on the model was addressed through the use of PCC analysis to exclude two auxiliary variables, DEM and NDVI₁₆. To assess the significance of this influence, both variables were reintroduced for a comparative analysis of the fusion results, as depicted in Fig. 17. The results obtained by removing DEM and NDVI₁₆ were labeled as 'Downscaling-r', while those incorporating DEM and NDVI₁₆ were labeled as 'Downscaling-a'. It is evident that, under the same conditions, Downscaling-r exhibits improvements across all evaluated aspects compared to Downscaling-a. Specifically, PCC increases by 1.30 %, while RMSE, MAE, and BIAS decrease by 2.50 %, 8.00 %, and 28.50 %, respectively. This improvement can be attributed to the relatively flat terrain in the study area, with ground gauge elevations being quite consistent. Furthermore, NDVI₁₆ demonstrated a hysteresis effect in response to precipitation. In summary, the removal of DEM and NDVI₁₆ enhanced the model's

performance. These findings underscore the significance of variable selection in the initial phase of the proposed method. Variables with low correlation to precipitation should be excluded to optimize the down-scaled model's performance.

5.3. Limitations and outlook

In this study, we generated a fused precipitation dataset using the GRASPS method, which combines three satellite precipitation datasets with ground gauge observations. In comparison to previous research on precipitation fusion, this dataset offers notable advantages in both spatial resolution and accuracy, particularly concerning extreme precipitation events (Zhang et al., 2023, Zhao et al., 2022). Our approach allowed us to obtain daily precipitation data at a high spatial resolution of 1 km, in contrast to most earlier studies, which typically achieved precipitation data at a spatial resolution of 0.25° (approximately 25 km). Furthermore, our generated dataset demonstrated strong performance in correcting extreme precipitation, whereas prior research primarily focused on overall precipitation correction.

Looking ahead, we anticipate further enhancements to this methodology. We believe that increasing the number of rain gauges will enhance the model's performance. In our study area, we had only 36 ground gauges (6 stations/10,000 km²), which was a limitation imposed by practical constraints. The accuracy of the results exhibited some variability across different land cover types. With access to more gauge data, we anticipate that this method will continue to be applicable and will yield even higher-quality data. We also explored this issue by comparing our approach to existing studies. Previous research achieved satisfactory results even with lower ground gauge densities (e.g., 1 station/10,000 km², 2 stations/10,000 km², and 0.8 stations/10,000 km²) (Chen et al., 2019, Wu et al., 2020, Zeng et al., 2022). Thus, our use of 36 sites to generate 3H precipitation data in this study was justified. Furthermore, there is potential for improving spatial and temporal resolutions. Highly accurate precipitation data at a daily scale and 1 km resolution are exceptionally valuable for the targeted WUA region in this study. As more ground data and satellite datasets become accessible, there is a strong likelihood that even higher spatial and temporal resolutions, including sub-daily scales and meter-level precision, can be achieved using the same methodology. When this happens, these fine-scale datasets will be invaluable for regional hydrology studies.

6. Conclusions

In this study, we introduced the GRASPS methodology as a downscaling fusion correction approach for multi-source precipitation data, leveraging Random Forest (RF) as the underlying algorithm. The GRASPS method initially performed spatial downscaling of three satellite precipitation datasets (IMERG, TMPA, and PERSIANN-CDR) in combination with cloud data. Subsequently, temporal data were integrated, and gauge precipitation observations were utilized for refinement. This comprehensive approach resulted in the creation of a high-resolution (1 km) 3H (High-precision, High-resolution, High-coverage) precipitation dataset characterized by exceptional accuracy (Overall PCC up to 0.77, RMSE and MAE less than 6.08 and 2.20 mm, respectively) and spatiotemporal continuity (daily and seamless spatial coverage) for the WUA during the year 2019. Comparing this 3H dataset with the original satellite precipitation datasets, it was apparent that the newly generated dataset incorporated their advantages while effectively correcting precipitation errors. The findings demonstrated notable consistency with site interpolation data. Through validation using data from 36 ground gauges, substantial improvements were observed across various spatial and temporal scales as indicated by the PCC, RMSE, and MAE indices. Moreover, the method exhibited exceptional performance in diverse land cover types, particularly in building areas. Among the fusion algorithms tested, Random Forest (RF) outperformed other

machine learning algorithms, such as Decision Tree (DT), Bagging, K-Nearest Neighbor (KNN), Adaboost, and Support Vector Machine (SVM), underscoring RF's advantages within the GRASPS framework. In summary, the precipitation dataset developed in this study offers highly detailed regional precipitation information with a spatial resolution of 1 km, daily temporal resolution, full spatial coverage, and superior accuracy. This high-quality precipitation data is crucial for researching regional hydrology and extreme events. In addition, it also provides important data support for extreme precipitation analysis and interpretation under climate change and urbanization and has great implications for guiding such an economically developed and densely populated urban agglomeration to deal with extreme precipitation events.

Conceptualization, X.Z. and Y.S.; methodology, X.Z., Y.S., and X.G.; software, T.H., Y.S. and W.-H.N.; Validation, S.H., J.Z., Y.Z., and D.N.; formal analysis, X.Z. and Z.Y.; investigation, X.Z., T.H. and Y.S.; resources, X.Z., and X.G.; data curation, T.H. and Y.S.; writing—original draft preparation, X.Z. and Y.S.; writing—review and editing, W.-H.N., X.G., J.Z., S.H., N.C., Y.Z., and D.N.; visualization, X.Z. and Y.S.; supervision, X.Z. and X.G.; project administration, X.Z. All authors have read and agreed to the published version of the manuscript.

Declaration of competing interest

The authors declare that they have no known competing financial interests or personal relationships that could have appeared to influence the work reported in this paper.

Data availability

Data will be made available on request.

Acknowledgments

This work was supported by grants from the Project Supported by the China National Key R&D Program (2023YFF0807000), the Open Fund of Hubei Luojia Laboratory (220100059), the Special Fund of Hubei Luojia Laboratory (220100034), the National Natural Science Foundation of China (U2340230 and 42371041), the Key R&D Program of Hubei province, China (2023BCB117 & 2023DJC154), Pre-research Project of SongShan Laboratory (No. YYYY062022001), the Open Fund of State Key Laboratory of Remote Sensing Science, China (OFSLRSS202114), and the Youth Innovation Promotion Association CAS (Grant No. Y2022050).

Appendix A

Figs. A1 – A5.

References

- Arkin, P.A., 1979. The Relationship between Fractional Coverage of High Cloud and Rainfall Accumulations during GATE over the B-Scale Array. *Monthly Weather Review* 107 (10), 1382–1387. [https://doi.org/10.1175/1520-0493\(1979\)107<1382:TRBFCO>2.0.CO;2](https://doi.org/10.1175/1520-0493(1979)107<1382:TRBFCO>2.0.CO;2).
- Arkin, P.A., Meisner, B.N., 1987. The Relationship between Large-Scale Convective Rainfall and Cold Cloud over the Western Hemisphere during 1982–84. *Monthly Weather Review* 115 (1), 51–74. [https://doi.org/10.1175/1520-0493\(1987\)115<0051:TRBLSC>2.0.CO;2](https://doi.org/10.1175/1520-0493(1987)115<0051:TRBLSC>2.0.CO;2).
- Ashouri, H., Hsu, K.-L., Sorooshian, S., Braithwaite, D.K., Knapp, K.R., Cecil, L.D., Nelson, B.R., Prat, O.P., 2015. PERSIANN-CDR: Daily Precipitation Climate Data Record from Multisatellite Observations for Hydrological and Climate Studies. *Bull. Amer. Meteorol. Soc.* 96 (1), 69–83. <https://doi.org/10.1175/bams-d-13-00068.1>.
- Baez-Villanueva, O.M., Zambrano-Bigiarini, M., Beck, H.E., McNamara, I., Ribbe, L., Nauditt, A., Birkel, C., Verbist, K., Giraldo-Osorio, J.D., Xuan Thinh, N., 2020. RF-MEP: A novel Random Forest method for merging gridded precipitation products and ground-based measurements. *Remote Sens. Environ.* 239 <https://doi.org/10.1016/j.rse.2019.111606>.
- Beck, H. E., A. I. J. M. van Dijk, V. Levizzani, J. Schellekens, D. G. Miralles, B. Martens and A. de Roo, 2017: MSWEP: 3-hourly 0.25° global gridded precipitation (1979–2015) by merging gauge, satellite, and reanalysis data. *Hydrol. Earth Syst. Sci.*, 21, 1, 589–615, <https://doi.org/10.5194/hess-21-589-2017>.
- Beck, H.E., Wood, E.F., Pan, M., Fisher, C.K., Miralles, D.G., van Dijk, A.I.J.M., McVicar, T.R., Adler, R.F., 2019. MSWEP V2 Global 3-Hourly 0.1 Precipitation: Methodology and Quantitative Assessment. *Bull. Amer. Meteorol. Soc.* 100, 3, 473–500. <https://doi.org/10.1175/BAMS-D-17-0138.1>.
- Cheema, M.J.M., Bastiaanssen, W.G.M., 2011. Local calibration of remotely sensed rainfall from the TRMM satellite for different periods and spatial scales in the Indus Basin. *Int. J. Remote. Sens.* 33 (8), 2603–2627. <https://doi.org/10.1080/01431161.2011.617397>.
- Chen, N., Li, R., Zhang, X., Yang, C., Wang, X., Zeng, L., Tang, S., Wang, W., Li, D., Niyogi, D., 2020. Drought propagation in Northern China Plain: A comparative analysis of GLDAS and MERRA-2 datasets. *J. Hydrol.* 588, 125026. <https://doi.org/10.1016/j.jhydrol.2020.125026>.
- Chen, S., Li, Q., Zhong, W., Wang, R., Chen, D., Pan, S., 2022. Improved Monitoring and Assessment of Meteorological Drought Based on Multi-Source Fused Precipitation Data. *Int. J. Environ. Res. Public Health* 19 (3), 1542. <https://doi.org/10.3390/ijerph19031542>.
- Chen, J., Wang, Z., Wu, X., Chen, X., Lai, C., Zeng, Z., Li, J., 2019. Accuracy evaluation of GPM multi-satellite precipitation products in the hydrological application over alpine and gorge regions with sparse rain gauge network. *Hydrology Research* 50 (6), 1710–1729. <https://doi.org/10.2166/nh.2019.133>.
- Chen, X., Zou, X., Zhang, Q., Zeng, H., Cui, T., 2021. Climate observation of the Three Gorges Region of the Yangtze River in 2019. *AOSL* 14 (3), 100026. <https://doi.org/10.1016/j.aosl.2020.100026>.
- Chivers, B.D., Wallbank, J., Cole, S.J., Sebek, O., Stanley, S., Fry, M., Leontidis, G., 2020. Imputation of missing sub-hourly precipitation data in a large sensor network: A machine learning approach. *J. Hydrol.* 588, 125126. <https://doi.org/10.1016/j.jhydrol.2020.125126>.
- Dai, X., Wang, L., Li, X., Gong, J., Cao, Q., 2023. Characteristics of the extreme precipitation and its impacts on ecosystem services in the Wuhan Urban Agglomeration. *Science of the Total Environment* 864, 161045. <https://doi.org/10.1016/j.scitotenv.2022.161045>.
- Du, Y., Wang, D., Zhu, J., Lin, Z., Zhong, Y., 2022. Intercomparison of multiple high-resolution precipitation products over China: Climatology and extremes. *Atmos. Res.* 278 <https://doi.org/10.1016/j.atmosres.2022.106342>.
- Duan, Z., Ren, Y., Liu, X., Lei, H., Hua, X., Shu, X., Zhou, L., 2022. A comprehensive comparison of data fusion approaches to multi-source precipitation observations: a case study in Sichuan province, China. *Environmental Monitoring and Assessment* 194 (6), 422. <https://doi.org/10.1007/s10661-022-10098-5>.
- Gan, F., Diao, X., Tan, K., Li, X., Cao, G., Zhong, X., Gao, Y., 2023. Error correction forIMERG precipitation estimates based on climatological adjustment combining the dry-wet season division and weight allocation. *J. Hydrol.* 624, 129890. <https://doi.org/10.1016/j.jhydrol.2023.129890>.
- Gu, X., Ye, L., Xin, Q., Zhang, C., Zeng, F., Nerantzaki, S.D., Papalexiou, S.M., 2022. Extreme Precipitation in China: A Review on Statistical Methods and Applications. *Adv. Water Resour.* 163, 104144. <https://doi.org/10.1016/j.advwatres.2022.104144>.
- Gunning, D., Stefk, M., Choi, J., Miller, T., Stumpf, S., Yang, G.Z., 2019. XAI-Explainable artificial intelligence. *Sci Robot* 4, 37. <https://doi.org/10.1126/scirobotics.ay7120>.
- Guo, X., Tian, L., 2022. Spatial patterns and possible mechanisms of precipitation changes in recent decades over and around the Tibetan Plateau in the context of intense warming and weakening winds. *Climate Dynamics* 59 (7), 2081–2102. <https://doi.org/10.1007/s00382-022-06197-1>.
- Guo, B., Zhang, J., Meng, X., Xu, T., Song, Y., 2020. Long-term spatio-temporal precipitation variations in China with precipitation surface interpolated by ANUSPLIN. *Scientific Reports* 10 (1), 1–17. <https://doi.org/10.1038/s41598-019-57078-3>.
- Hasan, M.M., Sharma, A., Mariethoz, G., Johnson, F., Seed, A., 2016. Improving radar rainfall estimation by merging point rainfall measurements within a model combination framework. *Adv. Water Resour.* 97, 205–218. <https://doi.org/10.1016/j.advwatres.2016.09.011>.
- Hersbach, H., Bell, P., Berrisford, G., Biavati, A., Horányi, J., Muñoz Sabater, J., Nicolas, C., Peubey, R., Radu, I., Rozum, D., Schepers, A., Simmons, C., Soci, D., Dee, D. and J.-N. Thépaut, 2018: ERA5 hourly data on single levels from 1979 to present. *C3S CDS*, <https://doi.org/10.24381/cds.adbb2d47>.
- Heymsfield, A., Bansemir, A., Wood, N.B., Liu, G., Tanelli, S., Sy, O.O., Poellot, M., Liu, C., 2018. Toward Improving Ice Water Content and Snow-Rate Retrievals from Radars. Part II: Results from Three Wavelength Radar-Collocated In Situ Measurements and CloudSat-GPM-TRMM Radar Data. *J. Appl. Meteorol. Climatol.* 57, 2, 365–389. <https://doi.org/10.1175/jamc-d-17-0164.1>.
- Huang, S., Zhang, X., Chen, N., Li, B., Ma, H., Xu, L., Li, R., Niyogi, D., 2021. Drought propagation modification after the construction of the Three Gorges Dam in the Yangtze River Basin. *J. Hydrol.* 603, 127138. <https://doi.org/10.1016/j.jhydrol.2021.127138>.
- Huang, S., Zhang, X., Chen, N., Ma, H., Fu, P., Dong, J., Gu, X., Nam, W.-H., Xu, L., Rab, G., Niyogi, D., 2022a. A Novel Fusion Method for Generating Surface Soil Moisture Data with High Accuracy, High Spatial Resolution, and High Spatio-Temporal Continuity. *Water. Resour. Res.* 58. <https://doi.org/10.1029/2021WR030827>.
- Huang, S., Zhang, X., Yang, L., Chen, N., Nam, W.-H., Niyogi, D., 2022b. Urbanization-induced drought modification: Example over the Yangtze River Basin, China. *Urban Climate* 44. <https://doi.org/10.1016/j.uclim.2022.101231>.
- Huffman, G.J., Bolvin, D.T., Nelkin, E.J., Wolff, D.B., Adler, R.F., Gu, G., Hong, Y., Bowman, K.P., Stocker, E.F., 2007. The TRMM Multisatellite Precipitation Analysis

- (TMPA): Quasi-Global, Multiyear, Combined-Sensor Precipitation Estimates at Fine Scales. *J. Hydrometeorol.* 8 (1), 38–55. <https://doi.org/10.1175/jhm560.1>.
- Huffman, G.J., Adler, R.F., Bolvin, D.T., Nelkin, E.J., 2010. The TRMM Multi-Satellite Precipitation Analysis (TMPA). Satellite Rainfall Applications for Surface Hydrology 3–22. https://doi.org/10.1007/978-90-481-2915-7_1.
- Huffman, G.J., E. F. Stocker, D. T. Bolvin, E. J. Nelkin and J. Tan, 2019: GPM IMERG Final Precipitation L3 1 day 0.1 degree x 0.1 degree V06. *GES DISC*, <https://doi.org/10.5067/GPM/IMERGDF/DAY/06>.
- Huffman, G.J. et al., 2020. Integrated Multi-satellite Retrievals for the Global Precipitation Measurement (GPM) Mission (IMERG). In: V. Levizzani et al. (V. Levizzani, C. Kidd, D. B. Kirschbaum, C. D. Kumarow, K. Nakamura and F. J. Turks), *Satellite Precipitation Measurement: 1*. Springer International Publishing, Cham, pp. 343–353. https://doi.org/10.1007/978-3-030-24568-9_19.
- Islam, M.A., Yu, B., Cartwright, N., 2020. Assessment and comparison of five satellite precipitation products in Australia. *J. Hydrol.* 590, 125474. <https://doi.org/10.1016/j.jhydrol.2020.125474>.
- Jia, S., Zhu, W., Lü, A., Yan, T., 2011. A statistical spatial downscaling algorithm of TRMM precipitation based on NDVI and DEM in the Qaidam Basin of China. *Remote Sens. Environ.* 115 (12), 3069–3079. <https://doi.org/10.1016/j.rse.2011.06.009>.
- Kotz, M., Levermann, A., Wenzl, L., 2022. The effect of rainfall changes on economic production. *Nature* 601 (7892), 223–227. <https://doi.org/10.1038/s41586-021-04283-8>.
- Krishnan, S., Pradhan, A., Indu, J., 2022. Estimation of high-resolution precipitation using downscaled satellite soil moisture and SM2RAIN approach. *J. Hydrol.* 610, 127926. <https://doi.org/10.1016/j.jhydrol.2022.127926>.
- Kunkel, K.E., Karl, T.R., Squires, M.F., Yin, X., Stegall, S.T., Easterling, D.R., 2020. Precipitation Extremes: Trends and Relationships with Average Precipitation and Precipitable Water in the Contiguous United States. *J. Appl. Meteor. Climatol.* 59 (1), 125–142. <https://doi.org/10.1175/jamc-d-19-01851>.
- Lei, H., Zhao, H., Ao, T., 2022. A two-step merging strategy for incorporating multi-source precipitation products and gauge observations using machine learning classification and regression over China. *Hydrol. Earth Syst. Sci.* 2022, 1–33. <https://doi.org/10.5194/hess-2021-642>.
- Lesk, C., Coffel, E., Horton, R., 2020. Net benefits to US soy and maize yields from intensifying hourly rainfall. *Nat. Clim. Change* 10 (9), 819–822. <https://doi.org/10.1038/s41558-020-0830-0>.
- Lin, C.-Y., Chen, W.-C., Chang, P.-L., Sheng, Y.-F., 2011. Impact of the Urban Heat Island Effect on Precipitation over a Complex Geographic Environment in Northern Taiwan. *J. Appl. Meteor. Climatol.* 50 (2), 339–353. <https://doi.org/10.1175/2010jamc2504.1>.
- Liu, K., Zhou, J., 2021. Main characteristics of climate and its impact on agriculture in Hubei province in 2019. *Hubei Agricultural Sciences* 60 (01), 37–41. <https://doi.org/10.14088/j.cnki.issn0439-8114.2021.01.008>.
- Liú, H., Zou, L., Xia, J., Chen, T., Wang, F., 2022. Impact assessment of climate change and urbanization on the nonstationarity of extreme precipitation: A case study in an urban agglomeration in the middle reaches of the Yangtze river. *Sustainable Cities and Society* 85, 104038. <https://doi.org/10.1016/j.scs.2022.104038>.
- Luo, M., Liu, T., Meng, F., Duan, Y., Bao, A., Frankl, A., De Maeyer, P., 2019. Spatiotemporal characteristics of future changes in precipitation and temperature in Central Asia. *International Journal of Climatology* 39 (3), 1571–1588. <https://doi.org/10.1002/joc.5901>.
- Ma, H., Zeng, J., Zhang, X., Fu, P., Zheng, D., Wigneron, J.-P., Chen, N., Niyyogi, D., 2021. Evaluation of six satellite- and model-based surface soil temperature datasets using global ground-based observations. *Remote Sens. Environ.* 264, 112605 <https://doi.org/10.1016/j.rse.2021.112605>.
- Manz, B., Buytaert, W., Zulkafli, Z., Lavado, W., Willem, B., Robles, L.A., Rodríguez-Sánchez, J.-P., 2016. High-resolution satellite-gauge merged precipitation climatologies of the Tropical Andes. *J. Geophys. Res.: Atmos.* 121, 3, 1190–1207. <https://doi.org/10.1002/2015JD023788>.
- Mokhtar, A., Jalali, M., He, H., Al-Ansari, N., Elbeltagi, A., Alsafadi, K., Abdo, H.G., Sammen, S.S., Gyasi-Agyei, Y., Rodrigo-Comino, J., 2021. Estimation of SPEI Meteorological Drought Using Machine Learning Algorithms. *IEEE Access* 9, 65503–65523. <https://doi.org/10.1109/access.2021.3074305>.
- Nerini, D., Zulkafli, Z., Wang, L.-P., Onof, C., Buytaert, W., Lavado-Casimiro, W., Guyot, J.-L., 2015. A Comparative Analysis of TRMM-Rain Gauge Data Merging Techniques at the Daily Time Scale for Distributed Rainfall-Runoff Modeling Applications. *J. Hydrometeorol.* 16 (5), 2153–2168. <https://doi.org/10.1175/jhm-d-14-0197.1>.
- Nguyen, P., Shearer, E.J., Tran, H., Ombadi, M., Hayatbini, N., Palacios, T., Huynh, P., Braithwaite, D., Updegraff, G., Hsu, K., Kuligowski, B., Logan, W.S., Sorooshian, S., 2019. The CHRS Data Portal, an easily accessible public repository for PERSIANN global satellite precipitation data. *Sci. Data* 6 (1), 180296. <https://doi.org/10.1038/sdata.2018.296>.
- Niu, Y., Touma, D., Ting, M., Camargo, S.J., Chen, R., 2022. Assessing heavy precipitation risk associated with tropical cyclones in China. *J. Appl. Meteor. Climatol.* <https://doi.org/10.1175/jamc-d-21-0166.1>.
- Parajuli, B., Zhang, X., Deuja, S., Liu, Y., 2021. Regional and Seasonal Precipitation and Drought Trends in Ganga-Brahmaputra Basin. *Water* 13 (16), 2218. <https://doi.org/10.3390/w13162218>.
- Peng, S., Ding, Y., Liu, W., Li, Z., 2019. 1km monthly temperature and precipitation dataset for China from 1901 to 2017. *Earth Syst. Sci. Data* 11 (4), 1931–1946. <https://doi.org/10.5194/essd-11-1931-2019>.
- Richards, F., Arkin, P., 1981. On the Relationship between Satellite-Observed Cloud Cover and Precipitation. *Monthly Weather Review* 109 (5), 1081–1093. [https://doi.org/10.1175/1520-0493\(1981\)109<1081:OTRBSO>2.0.CO;2](https://doi.org/10.1175/1520-0493(1981)109<1081:OTRBSO>2.0.CO;2).
- Sachindra, D.A., Ahmed, K., Rashid, M.M., Shahid, S., Perera, B.J.C., 2018. Statistical downscaling of precipitation using machine learning techniques. *Atmos. Res.* 212, 240–258. <https://doi.org/10.1016/j.atmosres.2018.05.022>.
- Sadeghi, M., Nguyen, P., Naeini, M.R., Hsu, K., Braithwaite, D., Sorooshian, S., 2021. PERSIANN-CCS-CDR, a 3-hourly 0.04° global precipitation climate data record for heavy precipitation studies. *Sci. Data* 8, 1, 157. <https://doi.org/10.1038/s41597-021-00940-9>.
- Sekararam, A.B., Masunaga, H., 2019. Origins of Heavy Precipitation Biases in the TRMM PR and TMI Products Assessed with CloudSat and Reanalysis Data. *J. Appl. Meteor. Climatol.* 58 (1), 37–54. <https://doi.org/10.1175/jamc-d-18-0011.1>.
- Senf, F., Dietzsch, F., Hünerbein, A., Denneke, H., 2015. Characterization of Initiation and Growth of Selected Severe Convective Storms over Central Europe with MSG-SEVIRI. *J. Appl. Meteor. Climatol.* 54 (1), 207–224. <https://doi.org/10.1175/jamc-d-14-0144.1>.
- Shen, G., Chen, N., Wang, W., Chen, Z., 2019. WHU-SGCC: a novel approach for blending daily satellite (CHIRP) and precipitation observations over the Jinsha River basin. *Earth Syst. Sci. Data* 11 (4), 1711–1744. <https://doi.org/10.5194/essd-11-1711-2019>.
- Shiru, M.S., Shahid, S., Dewan, A., Chung, E.-S., Alias, N., Ahmed, K., Hassan, Q.K., 2020. Projection of meteorological droughts in Nigeria during growing seasons under climate change scenarios. *Scientific Reports* 10 (1), 10107. <https://doi.org/10.1038/s41598-020-67146-8>.
- Sinclair, S., Pegram, G., 2005. Combining radar and rain gauge rainfall estimates using conditional merging. *Atmospheric Science Letters* 6 (1), 19–22. <https://doi.org/10.1002/asl.85>.
- Vandal, T., Kodra, E., Ganguly, A.R., 2019. Intercomparison of machine learning methods for statistical downscaling: the case of daily and extreme precipitation. *Theor. Appl. Climatol.* 137 (1), 557–570. <https://doi.org/10.1007/s00704-018-2613-3>.
- Wager, S., 2016. Comments on: A random forest guided tour. *TEST* 25 (2), 261–263. <https://doi.org/10.1007/s11749-016-0482-6>.
- Wang, H., Wang, G., Liu, L., 2018. Climatological Beam Propagation Conditions for China's Weather Radar Network. *J. Appl. Meteor. Climatol.* 57 (1), 3–14. <https://doi.org/10.1175/jamc-d-17-0097.1>.
- Wang, S., Zhang, X., Chen, N., Wang, W., 2022. Classifying diurnal changes of cyanobacterial blooms in Lake Taihu to identify hot patterns, seasons and hotspots based on hourly GOCI observations. *J. Environ. Manage.* 310, 114782 <https://doi.org/10.1016/j.jenvman.2022.114782>.
- Wang, S., Zhang, X., Wang, C., Chen, N., 2023a. Multivariable integrated risk assessment for cyanobacterial blooms in eutrophic lakes and its spatiotemporal characteristics. *Water Res* 228, Pt A, 119367. <https://doi.org/10.1016/j.watres.2022.119367>.
- Wang, S., Zhang, X., Wang, C., Chen, N., 2023b. Temporal continuous monitoring of cyanobacterial blooms in Lake Taihu at an hourly scale using machine learning. *Sci Total Environ* 857 (Pt 2), 159480. <https://doi.org/10.1016/j.scitotenv.2022.159480>.
- Wang, Y., Zhao, N., 2022. Evaluation of Eight High-Resolution Gridded Precipitation Products in the Heihe River Basin. Northwest China. *Remote Sens.* 14, 6. <https://doi.org/10.3390/rs14061458>.
- Wolfensberger, D., Gabella, M., Boscacci, M., Germann, U., Berne, A., 2021. RainForest: a random forest algorithm for quantitative precipitation estimation over Switzerland. *Atmos. Meas. Tech.* 14 (4), 3169–3193. <https://doi.org/10.5194/amt-14-3169-2021>.
- Wu, H., Yang, Q., Liu, J., Wang, G., 2020. A spatiotemporal deep fusion model for merging satellite and gauge precipitation in China. *J. Hydrol.* 584. <https://doi.org/10.1016/j.jhydrol.2020.124664>.
- Xiong, L., Liu, C., Chen, S., Zha, X., Ma, Q., 2021. Review of post-processing research for remote-sensing precipitation products. *Adv. Water. Resour.* 32 (4), 627. <https://doi.org/10.101402/j.cnki.32.1309.2021.04.014>.
- Xu, L., Chen, N., Moradkhani, H., Zhang, X., Hu, C., 2020a. Improving Global Monthly and Daily Precipitation Estimation by Fusing Gauge Observations, Remote Sensing, and Reanalysis Data Sets. *Water. Resour. Res.* 56, 3. <https://doi.org/10.1029/2019wr026444>.
- Xu, L., Zhang, C., Chen, N., Hamid, M., Chu, P.-S., Xiang, Z., 2020b. Potential Precipitation Predictability Decreases Under Future Warming. *Geophys. Res. Lett.* 47 <https://doi.org/10.1029/2020GL090798>.
- Xu, L., Chen, N., Zhang, X., Moradkhani, H., Zhang, C., Hu, C., 2021. In-situ and triple-collocation based evaluations of eight global root zone soil moisture products. *Remote Sens. Environ.* 254, 112248 <https://doi.org/10.1016/j.rse.2020.112248>.
- Yan, X., Chen, H., Tian, B., Sheng, S., Wang, J., Kim, J.-S., 2021. A Downscaling-Merging Scheme for Improving Daily Spatial Precipitation Estimates Based on Random Forest and Cokriging. *Remote Sens.* 13, 11. <https://doi.org/10.3390/rs13112040>.
- Yan, Z., Wang, J., Xia, J., Feng, J., 2016. Review of recent studies of the climatic effects of urbanization in China. *Adv. Clim. Changes* 7 (3), 154–168. <https://doi.org/10.1016/j.accre.2016.09.003>.
- Yuan, Y., Zhai, P., 2022. Latest understanding of extreme weather and climate events under global warming and urbanization influences. *Transactions of Atmospheric Sciences* 467. <https://doi.org/10.13878/j.cnki.dqkxxb.20211011001>.
- Zandi, O., Zahraie, B., Nasseri, M., Behrang, A., 2022. Stacking machine learning models versus a locally weighted linear model to generate high-resolution monthly precipitation over a topographically complex area. *Atmos. Res.* 272, 106159 <https://doi.org/10.1016/j.atmosres.2022.106159>.
- Zeng, Z., Chen, H., Shi, Q., Li, J., 2022. Spatial Downscaling of IMERG Considering Vegetation Index Based on Adaptive Lag Phase. *IEEE Trans. Geosci. Electron.* 60, 1–15. <https://doi.org/10.1109/tgrs.2021.3070417>.
- Zhan, C., Chen, Y., Yang, K., Zhou, X., Jiang, Y., Ling, X., Tian, J., Wang, Y., Li, X., Yang, H., 2023. First evaluation of GPM-Era satellite precipitation products with new

- observations on the western Tibetan Plateau. *Atmos. Res.* 283, 106559. <https://doi.org/10.1016/j.atmosres.2022.106559>.
- Zhang, T., Li, B., Yuan, Y., Gao, X., Sun, Q., Xu, L., Jiang, Y., 2018. Spatial downscaling of TRMM precipitation data considering the impacts of macro-geographical factors and local elevation in the Three-River Headwaters Region. *Remote Sens. Environ.* 215, 109–127. <https://doi.org/10.1016/j.rse.2018.06.004>.
- Zhang, T., Liang, Z., Wang, H., Wang, J., Hu, Y., Li, B., 2023. Merging multisatellite precipitation products using stacking method and the censored-shifted gamma ensemble model output statistics in china's Beimiaoji basin. *J. Hydrol.* 618, 129263. <https://doi.org/10.1016/j.jhydrol.2023.129263>.
- Zhang, Y.S., Wu, K., Zhang, J.L., Zhang, F., Xiao, H.X., Wang, F.C., Zhou, J.Y., Song, Y., Peng, L., 2021. Estimating Rainfall with Multi-Resource Data over East Asia Based on Machine Learning. *Remote Sens.* 13 (16), 3332. <https://doi.org/10.3390/rs13163332>.
- Zhao, Y., Xu, K., Dong, N., Wang, H., 2022. Optimally integrating multi-source products for improving long series precipitation precision by using machine learning methods. *J. Hydrol.* 609, 127707. <https://doi.org/10.1016/j.jhydrol.2022.127707>.